Methane to methanol: structure-activity relationships for Cu-CHA

Dimitrios K. Pappas[1], Elisa Borfecchia*[2,3], Michael Dyballa[1], Ilia A. Pankin[3,4], Kirill A. Lomachenko[4,5], Andrea Martini[3], Matteo Signorile[3], Shewangizaw Teketel[2], Bjørnar Arstad[6], Gloria Berlier[3], Carlo Lamberti[3,4], Silvia Bordiga[1,3], Unni Olsbye[1], Karl Petter Lillerud[1], Stian Svelle*[1] and Pablo Beato*[2]

[1]Center for Materials Science and Nanotechnology (SMN), Department of Chemistry, University of Oslo, 1033 Blindern, 0315 Oslo (Norway)

[2]Haldor Topsøe A/S, Haldor Topsøes Allé 1, 2800 Kongens Lyngby (Denmark)

[3]Department of Chemistry and INSTM Reference Center, University of Turin, via P. Giuria 7, 10125 Turin (Italy)

[4]IRC "Smart Materials", Southern Federal University, Zorge Street 5, 344090 Rostov-on-Don, (Russia)

[5]European Synchrotron Radiation Facility (ESRF), 71 avenue des Martyrs, CS 40220, 38043 Grenoble Cedex 9, (France)

[6]SINTEF Materials and Chemistry, Forskningsveien 1, 0373 Oslo (Norway)

ABSTRACT: Cu-exchanged zeolites possess active sites able to cleave the C−H bond of methane at temperatures ≤200 °C, enabling its selective partial oxidation to methanol. Herein we explore this process over Cu-SSZ-13 materials. We combine activity tests and X-Ray Absorption Spectroscopy (XAS) to thoroughly investigate the influence of reaction parameters and material elemental composition on the productivity and Cu-speciation during the key process steps. We find that the Cu^{II} moieties responsible for the conversion are formed in the presence of O_2 and that high temperature together with prolonged activation time increases the population of such active sites. We evidence a linear correlation between the reducibility of the materials and their methanol productivity. By optimizing the process conditions and material composition, we are able to reach a methanol productivity as high as 0.2 $molCH_3OH/molCu$ (125 µmol/g), the highest value reported to date for Cu-SSZ-13. Our results clearly demonstrate that high populations of 2Al Z_2Cu^{II} sites in 6r, favored at low values of both Si:Al and Cu:Al ratios, inhibit the material performance by being inactive for the conversion. $Z[Cu^{II}OH]$ complexes, although shown to be inactive, are identified as the precursors to the methane-converting active sites. By critical examination of the reported catalytic and spectroscopic evidences, we propose different possible routes for active site formation.

1. INTRODUCTION

The direct low-temperature conversion of methane to methanol is currently a heavily investigated field, due to its enormous potential for the energy and chemicals sector.[1-7] However, the high energy required for cleavage of the C−H bond in CH_4 combined with the facile over-oxidation to CO_x pose great challenges for the realization of such a process. In nature, mono-oxygenase enzymes in methanotrophic bacteria are able to transform methane to methanol.[8-10] These enzymes have inspired researchers in the field of heterogeneous catalysis to mimic such a unique reactivity. Metal-exchanged zeolites are able to stabilize well-defined metal-oxo sites: different zeolite topologies have been demonstrated to stabilize copper,[11-15] iron,[16-17] and other[18-19] metal-oxo clusters and all of them have shown activity for stoichiometric transformation of methane to methanol.

The ability of Cu-zeolites to selectively convert methane to methanol was evidenced for the first time by Groothaert and co-workers.[11] The authors proposed the methane C−H bond cleavage to occur over bis(μ-oxo) dicopper sites present in the pores of MFI (ZSM-5) and MOR frameworks. Following these findings, a wide range of zeolite frameworks have been investigated with MOR,[6, 11-15, 20-23] CHA,[15, 23-25] and MFI[11, 14, 26-27] exhibiting the highest yields of methanol.

Most reaction approaches found in the literature are based on a multi-step process, with an activation of the catalyst as the first step in order to generate the active sites. For the activation, H_2O_2,[16] N_2O,[24, 28] NO,[29] and O_2[11-15, 20-24, 26, 30] have led to the formation of Cu centers that were able to convert methane. Generally, a relatively low activation temperature (500 °C) combined with a cheap and available oxidant (i.e. air) would be preferred for forming the methane-converting centers in the zeolite. After this activation, methane is reacted over the material at different conditions (partial pressure, reaction time, and temperature) in order to cleave one C−H bond on the active sites. Finally, the product (methanol) is extracted using a polar solvent or by passing steam through the reactor. Recently, an alternative approach to this stepwise process was reported for Cu-MOR such that methane is fed at 7 bar and H_2O is utilized to partially oxidize methane and simultaneously regenerate the active sites while facilitating the product desorption.[6]

Apart from the process conditions, the methanol yield will obviously depend on the amount of copper present as active sites. However, the actual nature of the active Cu sites formed in different zeolites is still a heavily debated subject. For Cu-MOR, mono-(μ-oxo) dicopper sites have been proposed by Alayon et al.;[13, 31-32] isolated trimeric Cu-oxo centers have been suggested by Grund-

ner et al.,[12] and even larger Cu-oxo clusters have been discussed.[33-34] Recently, Cu-SSZ-13 has also been identified as an active material for the direct conversion of methane to methanol.[15, 23, 25] For Cu-SSZ-13, a zeolite with CHA topology, both monomeric active species, in the form of $[Cu^{II}OH]^+$ complexes,[35] and multimeric species[36] have been envisaged from theory. Ipek et al.[25] proposed the existence of $[Cu_2O_2]^{2+}$ and $[Cu_2O]^{2+}$ species in Cu-SSZ-13 zeolites based on PXRD, Raman and UV-Vis data, suggesting their involvement in the direct methane conversion.

Cu-exchanged SSZ-13 is also a highly efficient $deNO_x$ catalyst via NH_3-assisted Selective Catalytic Reduction (NH_3-SCR),[37-39] and has been extensively characterized in the literature, focusing on the Cu-species formed inside the zeolite lattice as a function of the temperature and gaseous environment,[25, 38-39] e.g. during thermal activation and into SCR-relevant conditions.[39-48]

Based on the extended knowledge accumulated in the context of NH_3-SCR over the past decade, and driven by the initial experimental insights about methane activation on Cu-SSZ-13,[15, 23-25] we identified this system as highly suited for establishing structure–activity relationships. Herein, we combine catalytic testing, *in situ*/*operando* X-ray Absorption Spectroscopy (XAS)[49] and complementary insights from Raman and FTIR spectroscopy to explore the methane to methanol conversion over Cu-SSZ-13 for a wide range of materials and reaction conditions. In doing so, optimization of the process conditions has been achieved, thereby arriving at the greatest reaction yield reported so far for this material. Moreover, a linear correlation between the amount of reducible Cu species and the reaction yield has been found.

2 RESULTS AND DISCUSSION

The Cu-SSZ-13 materials investigated in this work have been prepared by conventional aqueous ion exchange, and subjected to compositional and physico-chemical characterization by EDX, N_2-physisorption, SEM and PXRD. Additional details on the synthesis and laboratory characterization can be found in the Supporting Information (SI), Sections 1 and 2, respectively. The studied materials are named using ('Cu:Al')Cu-SSZ-13('Si:Al') code, to identify their composition.

We will first describe the effects of reaction conditions in the different steps of the process. Then, we will investigate the effect of characteristic pretreatments on the speciation via XAS and performance and follow the entire process with operando XAS. XAS measurements were carried out at the BM23[50] and BM26A[51] beamlines of the European Synchrotron Radiation Facility (ESRF) (for experimental details see SI, Section 1.4). Testing experiments were performed in our home laboratory, at comparable conditions in a standard fixed bed setup (for experimental details see SI, Section 1.3). Finally, the effects of material composition on productivity are explored. Complementary spectroscopic techniques, such as Raman and Fourier Transformed Infra-Red (FTIR) are utilized to assist the formulation of a complete scheme critically considering different active species as well as their formation mechanisms based on our observations and findings from the literature.

2.1 Impact of reaction parameters on the performance

High temperature activation of Cu-exchanged zeolites in oxygen-containing atmosphere is the initial step for the conversion. Temperature, oxygen partial pressure and time have been reported to strongly impact the Cu speciation in the materials[30, 40, 47, 52] and therefore they are also expected to have an effect on the methanol productivity. Recently, Kim et al. explored the effect of different oxidants in the activation process and showed that, in the case of O_2, 500 °C is a limit for Cu-MOR catalysts,[52] while Park et al. studied the effect of activation temperature over numerous structures finding a volcano-like behavior at 450 °C for most.[53] Here, we first study the effect of temperature, partial pressure and time during the oxygen activation step on the productivity over 0.5Cu-SSZ-13(12).

Figure 1a shows a linear dependency of the methanol productivity on the activation temperature. Moving from 350 to 500 °C, an increase of 160% in the methanol output was observed, reaching a productivity equal to 0.041 $molCH_3OH/molCu$ (25.3 µmol/g) with 86% selectivity. The selectivity remained approximately constant over the entire activation temperature range. Further, the material was activated at 450 °C for 120 min with the partial pressure of O_2 ranging from 0 to 1000 mbar (Figure 1b). Increasing the oxygen partial pressure from 67 to 187 mbar leads to a uniform increase of the productivity, which then levels to 0.038 $molCH_3OH/molCu$ (23.2 µmol/g) at higher partial pressures. Activation of the material in pure He at 450 °C (first point in Figure 1b) resulted in very low productivity of 0.014 $molCH_3OH/molCu$. Looking into the effect of activation time (Figure 1c) it is observed that increasing the activation time from 60 to 480 min results in an increase of the methanol yield by almost 100 %. After 480 minutes of activation, a plateau is observed, corroborating the fact that the activation process requires time to reach an optimum at these conditions (187 mbar O_2 and at 450 °C). The maximum productivity is observed after 720 minutes of activation, 0.058 $molCH_3OH/molCu$ (35.8 µmol/g). These results show that increased activation time, oxygen partial pressure, and reaction time all promote the population of Cu species responsible for the cleavage of the C−H bond of methane. The maximum methanol yield is 0.065 $molCH_3OH/molCu$ (40.6 µmol/g) and is reached when the sample is activated in pure oxygen at 500 °C for 480 min.

Looking into the methane loading step, initially we introduced 100 mbar of methane at different temperatures, for 60 min (Figure 1d). Loading methane at temperatures lower than 135 °C results in a very low productivity; a 35 °C increase in the temperature yields a roughly doubled output. A temperature of 200 °C is optimal for activation of methane; the corresponding productivity is equal to 0.034 $molCH_3OH/molCu$ (21.3 µmol/g) with a selectivity of 86%. Increasing the temperature up to 300 °C does not affect the total productivity, as the sum of the products remains constant. However, a significant decrease in selectivity is observed, since more CO_x is detected, leading to 63% selectivity at 300 °C. As mentioned before, the quantification of the products is obtained during the H_2O-assisted extraction step, so that the resulting CO_x might originate from different intermediates, such as formate, which evolve during the methane loading step. It appears that such species leading to full oxidation are favored at higher temperature. Moreover, a further rise of the temperature to 300-400 °C results in a decreased methanol and total productivity, indicating that high temperature hinders the stabilization of intermediates on the active centers. Figure 1e depicts the effect of CH_4 partial pressure on the productivity. The productivity doubled moving from 100 mbar (0.034 $molCH_3OH/molCu$) to 1000 mbar (0.061

molCH3OH/molCu). The higher CH_4 pressure leads to a greater coverage of activated species from methane. A similar trend has been observed over Cu-MOR zeolites for high-pressure methane loading, where an increased CH_4 pressure is suggested to transform spectator species into species that participate in the bond cleavage.[7] Finally the effect of contact time for 100 mbar CH_4 flow at 200 °C was explored. The results, in Figure 1f, show an increase in productivity from 30 min to 120 min, reaching 0.047 molCH3OH/molCu (38.0 µmol/g). Further increasing the time leads to a moderate rise in productivity, and a plateau is observed after ca. 300 min, at 0.058 molCH3OH/molCu.
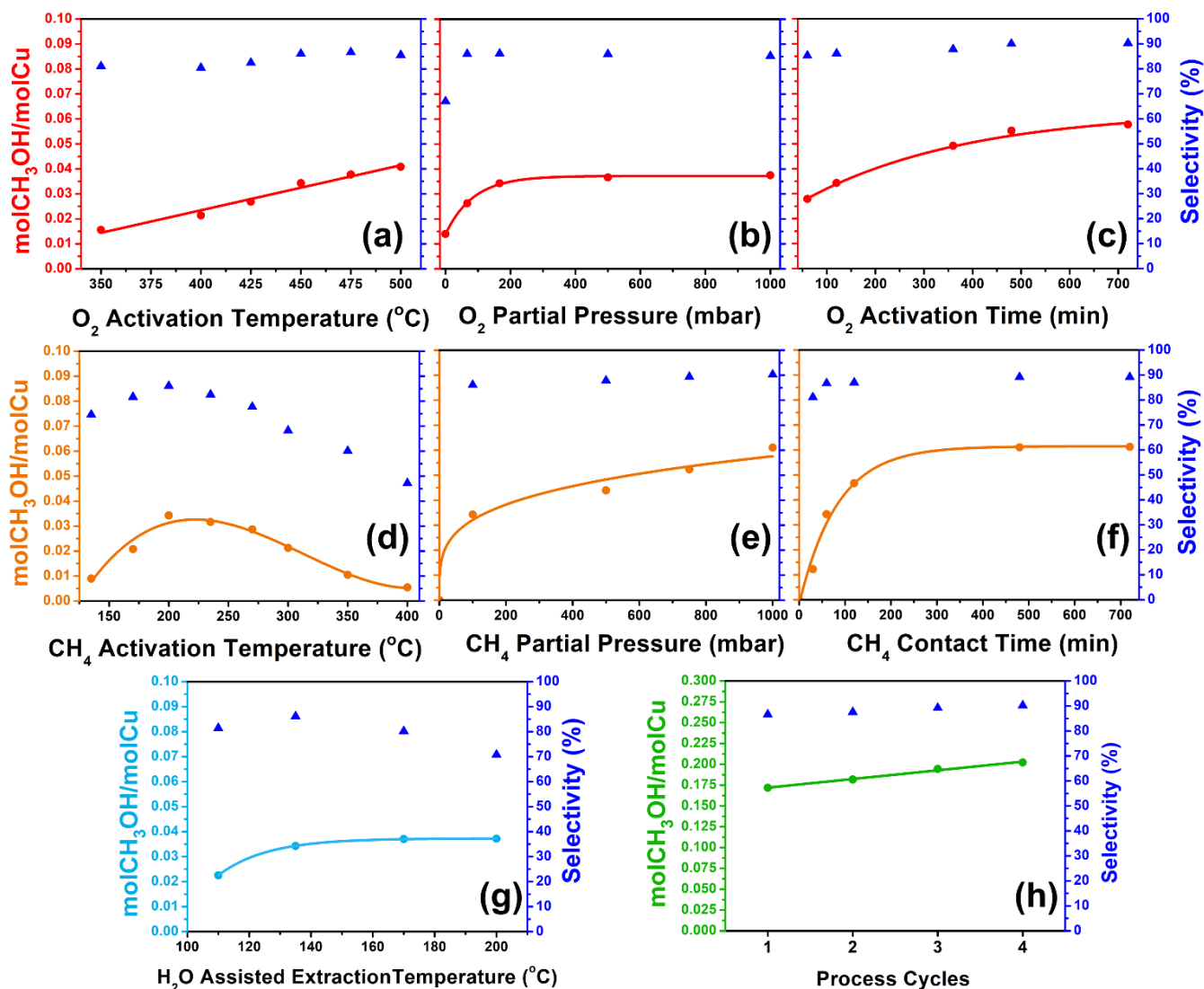

Figure 1. Normalized methanol productivity (molCH3OH/molCu - circles) and selectivity (% - triangles) during different reaction conditions and multiple cycles. Figures a-g follow the reference reaction conditions (i.e. O_2 activation: 450 °C for 120 min in 187 mbar O2, CH_4 loading: 60 min in 100 mbar CH_4 at 200 °C and H_2O assisted extraction: online with a 10% H_2O stream at 135 °C) while for each a single parameter is studied: (a) O_2 activation temperature; (b) O_2 partial pressure; (c) O_2 activation time, (d) CH_4, loading temperature; (e) CH_4 partial pressure; (g) CH_4 contact time; (g) H_2O assisted extraction temperature. Figure h shows the effect of reaction conditions for achieving the highest productivity (i.e. O_2 activation: 500 °C for 480 min in 1000 mbar O2, CH_4 loading: 360 min in 1000 mbar CH_4 at 200 °C and H_2O assisted extraction: online with a 10% H_2O stream at 200 °C) and the effect of multiple cycles of the process. Solid lines in the figure are utilized as a guide to the eye.

The final step of the process is the H_2O-assisted extraction of methanol. Passing 10% steam (in He) through the fixed bed reactor, the selectively oxidized products (i.e. methanol and dimethyl ether, accounted as two methanol molecules) are extracted along with over-oxidized CO_x species. Prior to extraction, the sample was exposed to reference reaction conditions (see SI, Section 3). Figure 1g shows productivity and selectivity obtained by performing the extraction at temperatures ranging from 110 to 200 °C. A temperature above 135 °C is required to fully desorb methanol within the fixed time. When raising the temperature, an increase in the total productivity is observed, indicating that a higher extraction temperature favors the desorption of adsorbed C-containing species in the form of over-oxidation products, as the methanol yield is constant. In particular, comparing extraction at 135 and 200 °C, a constant methanol yield of 0.037 molCH3OH/molCu (23.1 µmol/g) is observed, whereas the selectivity decreases from 86 to 70%.

From a process-design perspective, the constant yield over this broad temperature range is an important feature, since it potentially allows methane loading and methanol extraction to be operated isothermally at 200 °C.

The evaluation of the individual reaction parameters was translated into optimized conditions and applied in multiple process cycles. Activation at 500 °C for 480 min in a 1000 mbar O_2 feed, followed by methane loading at 200 °C for 360 min in a 1000 mbar CH_4 feed, and a H_2O-assisted extraction of methanol at 200 °C (see also SI, Section 3) yield 0.172 molCH$_3$/molCu (107 µmol/g), the highest value reported so far for Cu-CHA zeolites. After completion of the first process cycle, the material was purged in He, at 200 °C and subsequently subjected to in total four complete cycles (Figure 1h). Interestingly, productivity and selectivity gradually increase after each process cycle. After four cycles, the methanol productivity reaches 0.202 molCH$_3$OH/molCu (125 µmol/g), a 17 % increase compared to the first cycle. An increase in productivity during successive process cycles has also been observed for Cu-exchanged MOR zeolites.[20, 30]

2.2 Impact of activation conditions on the XAS spectroscopic fingerprints

In the previous section, we demonstrated that temperature, oxygen partial pressure, and activation time have an impact on the methanol productivity of the 0.5Cu-SSZ-13(12). We characterized the material by XAS after four different pretreatments, namely (i) standard O_2-activation at 500 °C, (ii) activation in He at 500 °C, (iii, iv) activation in He at 500 °C followed by reaction with O_2, either at 500 °C or at 200 °C. The productivity was determined by contacting the sample with 1000 mbar of CH_4 at 200 °C for 60 min, followed by steam-assisted extraction of the products at 135 °C in a laboratory fixed bed reactor in order to identify Cu-speciation ↔ performance relationships.

The characteristic XANES features detected after the different activation protocols can be interpreted based on previous Cu K-edge XANES studies in Cu-zeolites[32, 40-41, 45, 47, 54-57] and Cu-containing enzymes.[58-60] XAS for the O_2-activated material at 500 °C (Figure 2, red curves) indicates a virtually pure Cu^{II} state.[40-41, 47] In the XANES, a pronounced rising-edge shoulder is observed in the 8985–8990 eV range, assigned to 1s → 4p transitions in three-/four-fold coordinated Cu^{II} sites. The weak pre-edge peak, arising from the dipole-forbidden 1s → 3d transition in d^9 Cu^{II} ions, is also well evident. Within the spectral resolution of our data, no evidence of Cu^{I} species is found after the O_2-activation step.

The k^2-weighted, phase uncorrected, Fourier transform of the EXAFS spectrum (hereafter FT-EXAFS) collected at 500 °C after O_2-activation shows three well defined maxima, peaking at ca. 1.4, 2.4, and 3.2 Å. These are seen throughout the entire stepwise methane conversion process, with modifications in their intensity (see Section 2.3). EXAFS fitting (see SI, Section 5.1) reveals that the first maximum derives from Cu-O single scattering (SS) paths involving two framework (O_{fw}) and one extra-framework (O_{ef}) oxygen in the first coordination shell of Cu, at (1.97 ± 0.04) Å and (1.86 ± 0.05) Å, respectively. In line with previous EXAFS studies on Cu-SSZ-13, the second maximum is assigned to the SS path involving a second-shell Al atom (T_{fw}) in framework-coordinated Cu-species,[45, 47, 61] here refined at Cu-T_{fw} = (2.72 ± 0.02) Å. Differently to what was proposed for Cu-MOR[31] and Cu-ZSM-5,[57] no significant contribution from Cu-Cu SS paths is found in this R-space range for Cu-SSZ-13. Conversely, considering the lack of other important scattering contributions in this R-space range, we associate the third maximum in the FT-EXAFS spectra with neighboring Cu sites in Cu_xO_y moieties, best-fitted to average metal-metal separation of (3.41 ± 0.06) Å. The FT-EXAFS spectra in Figure 2b are also reported in Figure S13 in an extended R-space range up to ca. 6 Å. Here, the weak peak at 3.4 Å can be clearly distinguished from the noise, dominating the spectra for R > 3.7 Å. Noteworthy, the experimental conditions employed here (activation up to 500 °C in pure O_2) yielded a more pronounced third maximum in comparison with our previous study mentioned before[40] conducted on a Cu-SSZ-13 zeolite with very similar composition (Si:Al ≈ 13; Cu:Al ≈ 0.44) but by activating the material only up to 400 °C in 50% O_2/He.

When Cu-SSZ-13 is pretreated in He at 500 °C (Figure 2, black lines), the overall XANES spectral shape is representative of a dominant Cu^{I} state. The characteristic Cu^{I} 1s → 4p peak at 8982.5 eV is evident, while the pre-edge peak is significantly reduced. Indeed, high-temperature treatment in inert gas is known to trigger, from ∼ 230 °C upward, the so called 'self-reduction' from Cu^{II} to Cu^{I}.[31, 40, 47, 54, 62-63] In the corresponding FT-EXAFS spectrum, we observe a lower intensity in the whole range, supporting the observations from XANES. Indeed, this state mostly consists of 'bare' ZCu^{I} ions (where Z indicates coordination to O_{fw} next to one isolated Al in a framework T-site, i.e. *1Al* site) in both *6r* and *8r* of the CHA framework.[40, 64-65] Both are twofold-coordinated sites, but with different local environments in the second shell. Such heterogeneity, together with the higher mobility of Cu^{I} with respect to Cu^{II},[66] causes a broadened and dampened second-shell signal. After He-activation, the third maximum at ca. 3.2 Å, well evident after O_2-activation, becomes barely detectable.

The productivities observed after the two different pretreatments are 0.008 molCH$_3$OH/molCu (4.7 µmol/g) and 0.082 molCH$_3$OH/molCu (50.8 µmol/g) for He and O_2 activation, respectively (Figure 2c), clearly indicating a positive correlation between methanol yield and the existence of Cu^{II} species in the activated materials. Instead, a low productivity is seen when the pretreatment is carried out in the absence of O_2.

To decouple the high-temperature treatment in inert leading to dehydration and self-reduction of copper from the reaction with O_2 resulting in the oxidation of Cu^{I} species, we reacted the He-activated sample with O_2 for 30 min at 500 and 200 °C (bordeaux and blue curves/bars in Figure 2a-c).

The oxidation at 500 °C (subsequent to He activation at the same temperature) yields very similar XAS spectra compared to the sample activated directly in O_2. In addition, the productivity after the two different activations is almost equivalent, only differing by ca. 10 %. Nonetheless, as it can be clearly noted by looking at the first derivative of the XANES spectrum, a small amount of Cu^{I} is still present after the subsequent oxidation. The amount of the remaining Cu^{I} is ca. 10% of the total copper, which is in good agreement with the slightly lower productivity. After both O_2-activation and oxidation at 500°C, a higher third shell component is observed compared to the He-only activated sample.

4

Carrying out the reaction with O_2 at 200 °C (after He activation at 500 ºC) results in the same relative Cu^{II}/Cu^{I} abundance as observed at 500 °C: a dominant Cu^{II} state is formed, with a residual fraction of ca. 10% Cu^{I}, indicating that the same fraction of Cu^{I} species formed during inert treatment react with oxygen even at lower temperature. Although XAS evidences that the fraction of Cu^{II} species formed upon re-oxidation at 500 °C and 200 °C is equivalent, the methanol yield of 0.046 molCH₃OH/molCu for the low temperature oxidation is 45% lower. Hence, low temperature oxidation alters the balance between active and inactive Cu^{II} species.
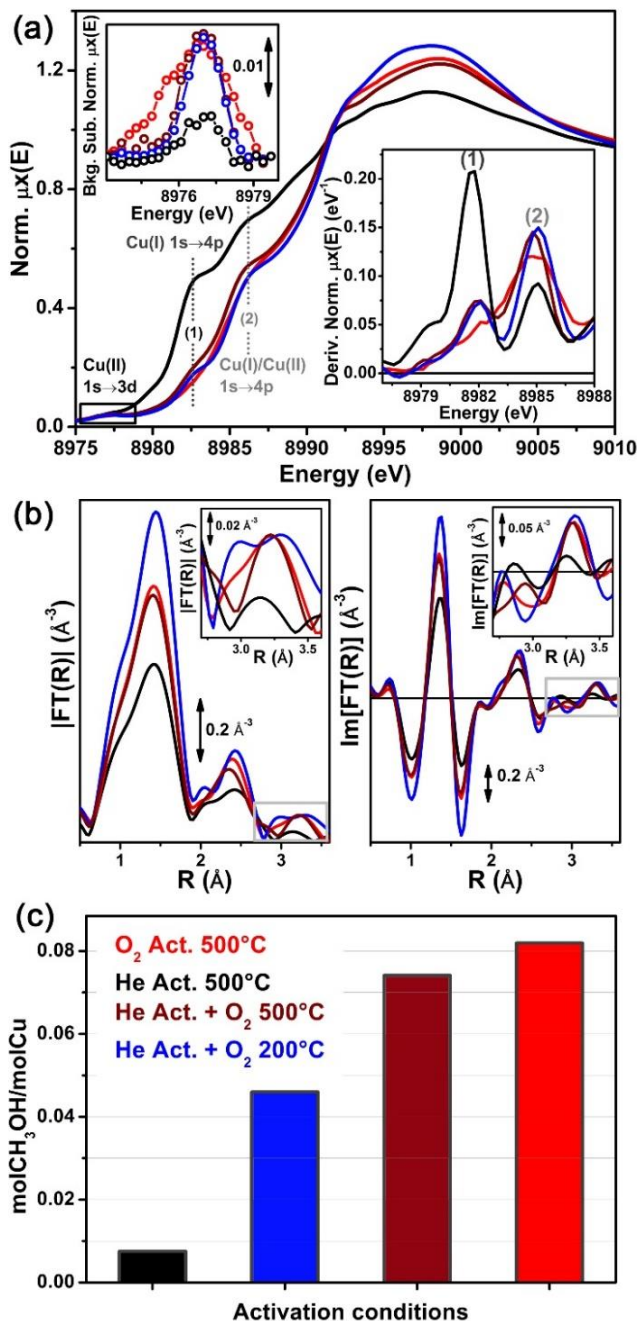
Figure 2. XAS characterization of the 0.5Cu-SSZ-13(12) after different pre-treatment and impact of the pre-treatment on productivity. (a) Main panel: Cu K-edge XANES spectra; left inset: background-subtracted Cu^{II} 1s → 3d pre-edge peak; right inset: first derivative of the XANES spectra reported in the main panel in the rising-edge region. Labels (1) and (2) refer to the rising-edge 1s → 4p peaks characteristic of Cu^{I} and Cu^{I}/Cu^{II} ions, respectively. (b) Magnitude (left) and imaginary part (right) of the FT-EXAFS spectra for the 0.5Cu-SSZ-13(12) after each pre-treatment, obtained by Fourier transforming the $k^2\chi(k)$ curves reported Figure S10a (SI) in the (2.4−10.8) Å⁻¹ range and using the same color code as in part (a). The insets report a magnification of the high-R region of FT-EXAFS spectra, highlighted by light gray boxes in the main panels. (c) Normalized methanol productivity (molCH₃OH/molCu) over the 0.5Cu-SSZ-13(12) in correspondence of each pre-treatment, followed by CH_4 activation at 200 °C for 60 min using 1000 mbar CH_4 feed, and H_2O assisted extraction at 135 °C.

Further comparing the XAS spectra of the material contacted with O_2 at 500 °C and 200 °C, significant differences in the average coordination environment of the Cu^{II} component are observed. In particular, oxidation at 200 °C yields a higher intensity of the

XANES white-line peak around 8998 eV and of the first-shell peak in the FT-EXAFS (beyond what is expected due to different acquisition temperature, see SI, Section 5.2 for details). Both these observations indicate a higher relative fraction of four-fold co-ordinated Cu^{II} sites formed when Cu^{I} is reacted with O_2 at 200 °C. The observed differences in coordination of Cu^{II} complexes, during direct O_2-activation and oxidation of a pre-reduced sample point to a temperature-dependent coordination preference: three-coordinated species are favored at 500 °C but undergo a partial conversion to four-coordinated species at 200 °C. If the reaction between Cu^{I} and O_2 is directly conducted at 200 °C, the preference towards four-coordinated Cu^{II} complexes appears more pronounced. The lower productivity observed in the latter conditions suggests that the tridentate coordination mode of Cu^{II} centers, with first-shell ligation to two O_{fw} and one O_{ef} atom, is most favorable for the active Cu site responsible of methane to methanol conversion in Cu-SSZ-13. Such a coordination mode is the one characteristic of Z[Cu^{II}OH] species, which are currently considered as the prototypes for redox-active framework-interacting Cu-sites in Cu-SSZ-13. Their presence after O_2-activation at 400 °C has been ascertained by *in situ* FTIR[40, 47, 67] detecting their υ(OH) fingerprint band at 3656 cm^{-1} and their high stability in the proximity of *1Al* sites in the 8r has been confirmed by DFT.[43, 47] Nevertheless, from the results discussed above, it is difficult to conceive that the Z[Cu^{II}OH] species are directly responsible for the CH_4 conversion, as it has been suggested theoretically.[35] In fact, significant populations of Z[Cu^{II}OH] species have been evidenced after both He and O_2 activation at 250 °C, i.e. when dehydration is completed and before the self-reduction process initiates (see also Section 2.5).[40, 64, 67] However, these kinds of pre-treatments do not yield significant methanol productivity (SI, Section 4).

2.3 Operando XAS of the complete process

We employed *operando* XAS to follow the oxidation state and average coordination of the Cu ions in the material during each step of the methane to methanol conversion over 0.5Cu-SSZ-13(12). Figure 3 shows the XANES and FT-EXAFS spectra collected after each step of the process, namely O_2-activation at 500 °C, He flush after cooling to 200 °C in O_2, CH_4-activation and H_2O-assisted extraction at 200 °C. Each FT-EXAFS spectrum was fitted as described in SI, Section 5.3, to evaluate average Cu coordination environment during the stepwise process. The procedure adopted for *operando* XAS experiments was adjusted to balance between the optimized process conditions and an effective exploitation of the beam-time. The exact experimental conditions as well as qualitative Mass Spectroscopy (MS) data collected during XAS experiment can be found in the SI. Such conditions resulted in an overall productivity of 0.100 molCH$_3$OH/molCu measured in a fixed bed reactor.

The XAS spectrum of O_2-activated 0.5Cu-SSZ-13(12) at 500 °C has been already described in detail in Section 2.2, and it is reported in Figure 3 (red curves) for comparison. After the high-temperature O_2-activation step, the sample was cooled down to 200 °C in O_2 and then flushed with He for 60 min. The XAS spectra collected at this stage depict the actual condition of the material before interaction with CH_4. From XANES, monitoring both the 1s→3d pre-edge peak and the rising-edge region, it is evident that the oxidation state of Cu remains unchanged. Nonetheless, XAS evidences an increased coordination number for the O_{ef} sub-shell, from 1.0 ± 0.5 to 1.3 ± 0.5. The modifications observed after cooling to 200 °C are very similar to what was noted in Section 2.2, when, comparing the XAS spectra of the material after oxidation at 500 and 200 °C. Indeed, a significant increase in the XANES white-line region is observed, accompanied by a 27% increase in the intensity of the first-shell peak in the FT-EXAFS spectrum with respect to the O_2-activated state at 500 °C. Such spectral changes are beyond what would be expected solely due to the decreased thermal contribution to Debye-Waller (DW) factors when lowering the temperature from 500 to 200 °C (see SI, Section 5.2). Concomitantly, the second- and third-shell regions are less perturbed, suggesting that, on average, the coordination mode to the zeolite framework is retained and that multimeric moieties formed during high-temperature O_2-activation are still intact.

Similarly to what has been previously reported for Cu-MOR,[31-32] loading of methane at 200 °C on Cu-SSZ-13 results in the partial reduction of Cu^{II} to Cu^{I}, as indicated by the development of a rising-edge peak around 8983 eV. In parallel, the 1s→ 3d peak undergoes a ca. 35% intensity decrease with respect to what was observed after He flush at 200 °C, confirming the reduction upon interaction with CH_4. As described in SI Section 5.4, we applied linear combination fit (LCF) analysis to obtain quantitative insights into Cu-speciation during interaction with CH_4. LCF evidences the formation of 27% Cu^{I} species, together with a small fraction (ca. 7%) of hydrated Cu^{II} complexes (see Figure 3d). In the FT-EXAFS (Figure 3b,c), interaction with CH_4 causes a slight decrease in the intensity of the first maximum, in line with a diminished first-shell coordination number in the newly formed Cu^{I} species ($N_{O(fw)}$ lowers from 2.0 to 1.6 after methane loading), whereas in the range from 2.0 to 3.5 Å only minor changes can be observed. The reduction of Cu-species after methane activation can, on the one hand, result from the formation of the reactive intermediate, which, according to Sushkevich et al.,[6] could involve the stabilization of methoxy species on the active sites and the formation of new Brønsted sites. On the other hand, Cu^{I} formation can be connected to the formation of CO_x species from O_2-donating Cu-sites, prompting the CH_4 oxidation. Noteworthy, oxidation of CH_4 to CO_x would be reasonably accompanied by production of H_2, reported to induce a complete Cu^{II} to Cu^{I} reduction in both Cu-SSZ-13[47] and Cu-MOR.[32] H_2 has been indeed detected by MS during *operando* XAS, together with over-oxidation products (SI, Section 5.8).

Finally, H_2O-assisted methanol extraction (Figure 3, light blue curves) promotes the formation of a significant fraction of hydrated Cu^{II} species, yielding an intensity increase and shape change in the XANES white-line region, together with an enhancement of the first-shell intensity in the FT-EXAFS spectra with respect to the CH_4-activation step. Importantly, at the end of the extraction step, the well-defined second-shell peak appears to be partially degraded, which is in excellent agreement with the formation of a fraction of mobile Cu^{II} aquo-complexes, 24% from LCF. Conversely, the third-shell maximum is largely intact after 60 min in 10% H_2O/He flow at 200 °C. Based on these evidences, we propose that introduction of water during the methanol extraction provokes a detachment of Cu-ions from redox-inert positions. If multiple cycles of the process are run, the mobile Cu^{II}-aquo complexes[40, 47, 68] formed during extraction are then thermally decomposed and able to form new active sites during the O_2-activation step of the subsequent cycle, justifying the observed performance enhancement (see Figure 1h).
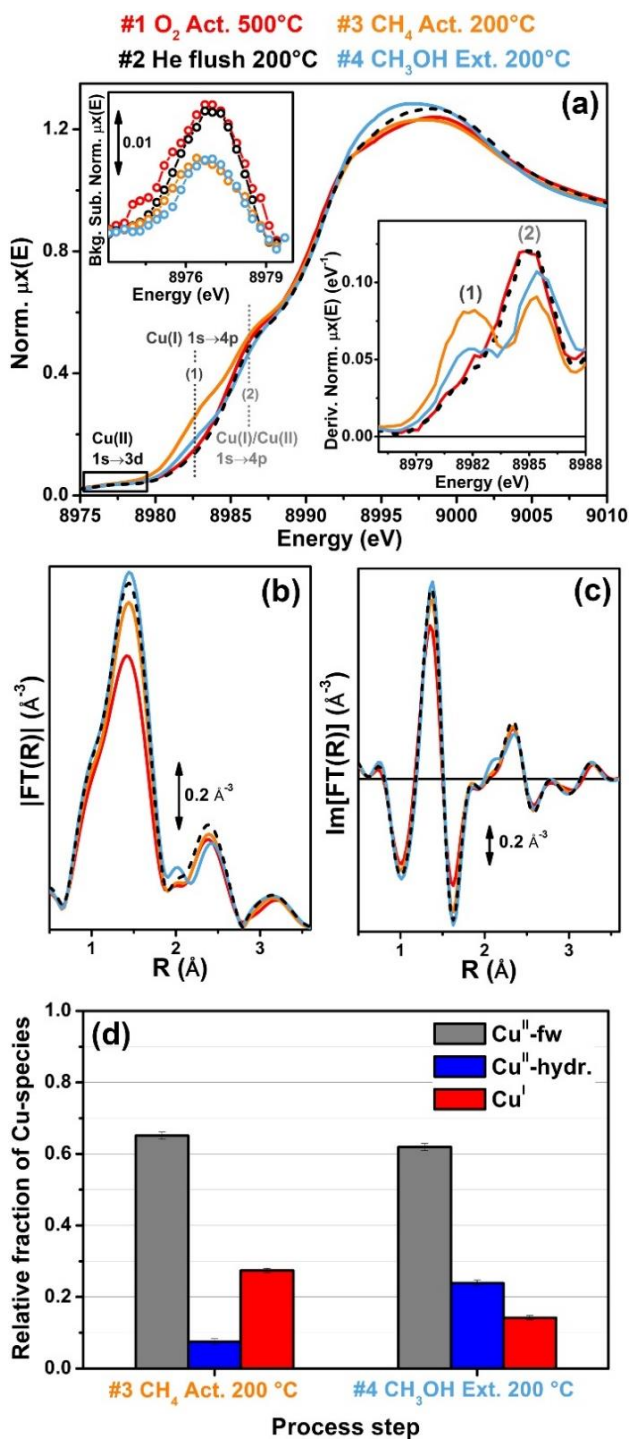
Figure 3. *Operando* XAS after each step of the methane conversion process: #1 O_2-activation at 500 °C; #2 He flush after cooling to 200 °C in O_2; #3 CH_4-activation at 200 °C; #4 H_2O-assisted CH_3OH extraction at 200 °C. (a) Main panel: Cu K-edge XANES spectra 0.5Cu-SSZ-13(12) after each process step; left inset: background-subtracted Cu^{II} 1s → 3d pre-edge peak; right inset: first derivative of the XANES spectra reported in the main panel in the rising-edge region. Labels (1) and (2) refer to the rising-edge 1s → 4p peaks characteristic of Cu^I and Cu^I/Cu^{II} ions, respectively. (b, c) Magnitude (b) and imaginary part (c) of the FT-EXAFS spectra of 0.5Cu-SSZ-13(12) after each process step, obtained by Fourier transforming the $k^2\chi(k)$ curves reported Figure S10b (SI) in the (2.4−10.8) Å^{-1} range. (d) Relative fractions of framework-interacting Cu^{II}, hydrated Cu^{II} and Cu^I species during steps #3 and step #4 derived from linear combination fit (LCF) of XANES spectra reported in part (a).

We also note that, albeit diminished with respect to the CH_4-activation step, a certain fraction of Cu^I is still present in the system: LCF indicates 14% of residual Cu^I at the end of the extraction step. By calculating the difference between the relative fractions of Cu^I present in the system after methane loading and extraction steps, we find 13% of total Cu to be re-oxidized during extraction, in good agreement with the corresponding productivity of 0.100 molCH_3OH/molCu. This correlation suggests that these Cu-species which undergo reduction when exposed to CH_4 and are re-oxidized when contacted with water, directly participate in the reaction.

2.4 Cu-SSZ-13 materials with different compositions

Having explored the effect of the different process parameters on the methanol yield and Cu-speciation for the 0.5Cu-SSZ-13(12), we extended our investigation to Cu-SSZ-13 samples with different elemental compositions (i.e. Cu:Al and Si:Al ratios).

Using the optimized process conditions (SI, Table S3), we evaluated samples with Cu:Al from 0.14 to 0.49, and constant Si:Al of 12 with respect to methanol productivity. Increasing the Cu content results in higher productivity per gram of sample, while selectivity remains constant at ca. 87 %. Additional insights can be obtained considering the normalized methanol productivity, reported in Figure 4a. Interestingly, at Cu:Al ~ 0.15 the output is significantly lower than for the higher-loading samples. Further increasing the Cu:Al ratio to ~ 0.5 only results in a slight increase in the normalized methanol yield, which reaches 0.172 molCH₃OH/molCu. Hence, the fraction of active species depends on the Cu-loading.

We also tested Cu-SSZ-13 materials with similar Cu:Al ratios (~ 0.5) at Si:Al ratios varying from 5 to 29. Not surprisingly, the methanol yields increase monotonically with the amount Cu per gram of sample, reaching 130 µmol/g for the Si:Al = 5 sample. However, normalization of these results with respect to the Cu loading leads to a rather different picture (Figure 4b), with the Si:Al = 12 sample showing the highest productivity among the four tested materials, equal to 0.172 molCH₃OH/molCu. In this comparison, the sample with the highest aluminum content reaches only a productivity of 0.112 molCH₃OH/molCu. Similar observations were reported also by Wulfers et al., evidencing a poorer performance for Cu-SSZ-13 zeolites with low Si:Al ratios.[15] For samples with Si:Al ratios of 12 and 15 we measured very similar normalized productivity, in line with the similar compositional characteristics. Conversely, increasing Si:Al to 29 results in a decrease of the productivity, down to 0.131 molCH₃OH/molCu.
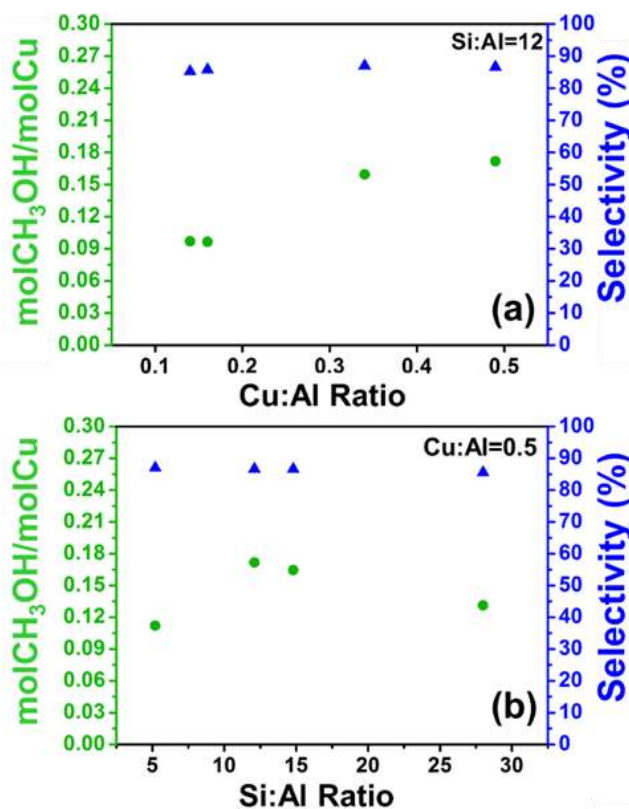

Figure 4. Productivity and selectivity for the methane to methanol conversion over Cu-SSZ-13 with different compositional characteristics evaluated utilizing the optimized process conditions (i.e. O₂ activation at 500 °C for 480 min in 1000 mbar O₂, CH₄ activation at 200 °C for 360 min using 1000 mbar CH₄ feed, H₂O assisted extraction at 200 °C) (a) normalized methanol productivity (molCH₃OH/molCu) as a function of Cu:Al ratio for Cu-SSZ-13 samples with Si:Al=12, (b) normalized methanol productivity (molCH₃OH/molCu) as a function of Si:Al ratio for Cu-SSZ-13 samples with Cu:Al=0.5.

In order to interpret the normalized methanol yields derived from the samples with different Si:Al as a function of the Cu speciation in the pre-treated materials, we applied XAS. In Section 2.2 we have shown how O₂-activation and high-temperature reaction with O₂ of the He-activated state result in almost identical performance, thus yielding equivalent populations of active Cu-sites. This knowledge allows us to decouple the dehydration, self-reduction and re-oxidation steps and obtain an in-depth understanding of the underlying redox mechanisms. Figure 5a-c shows the XANES and FT-EXAFS spectra of He-activated Cu-SSZ-13 samples with fixed Cu:Al ratio of 0.5 and Si:Al ratios of 5, 15, 29, namely 0.5Cu-SSZ-13(5), 0.5Cu-SSZ-13(15) and 0.5Cu-SSZ-13(29). The corresponding spectra collected on the same materials after subsequent oxidation at 500 °C are reported in Figure 5d-f.

The XANES spectra of the He-activated samples always show the presence of a certain fraction of Cu^I, which however increases in the following order: Si:Al = 15 > 29 > 5. These results are in line with previous reports, demonstrating that the SSZ-13 framework provides two different cation sites, with markedly different redox barrier, namely redox-active *1Al* sites in the *8r* and redox inert *2Al* sites in the *6r*.[47, 69-70]
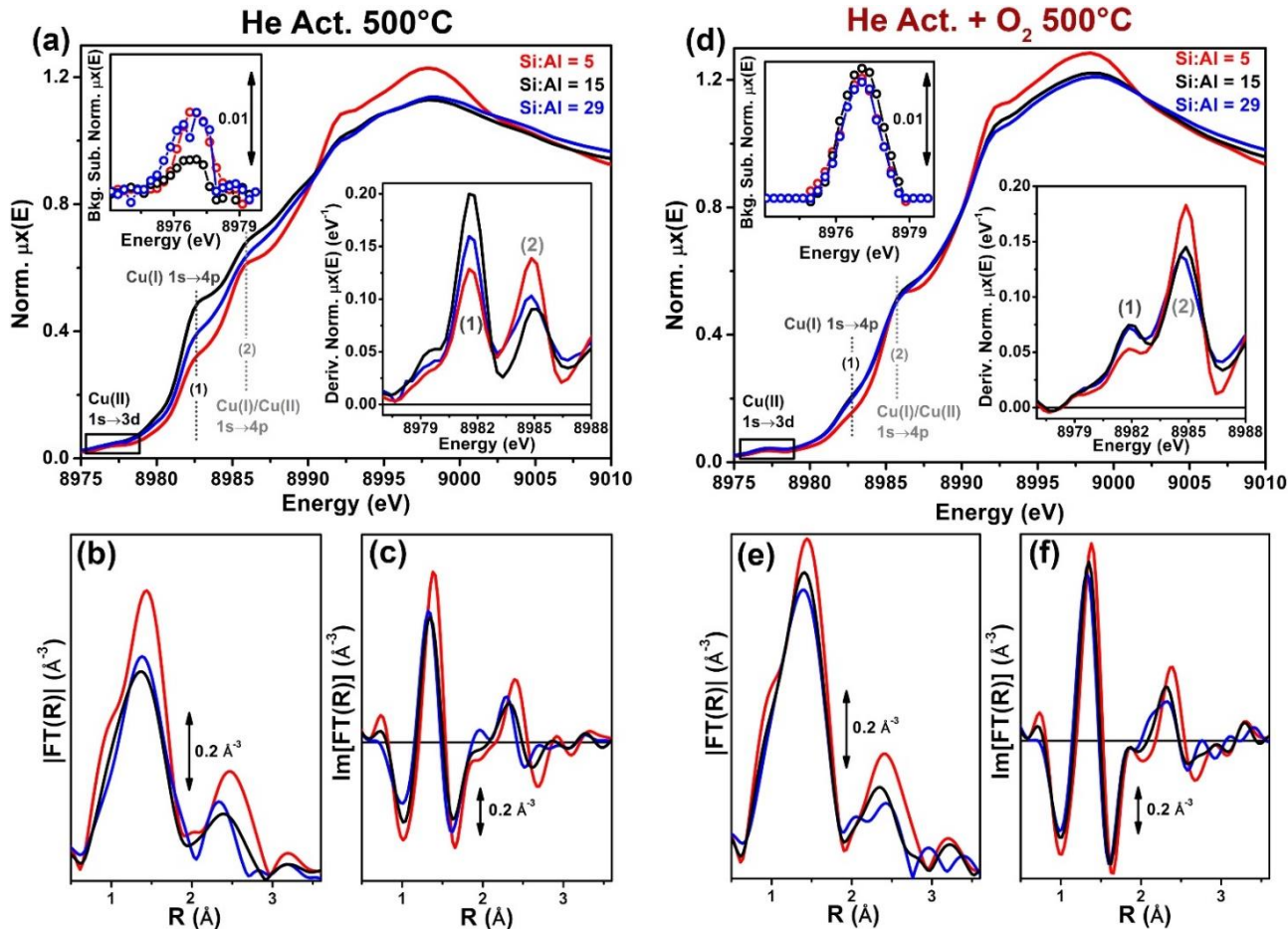
Figure 5. (a) Main panel: XANES spectra collected on 0.5Cu-SSZ-13(5) (red curves), 0.5Cu-SSZ-13(15) (black curves) and 0.5Cu-SSZ-13(29) (blue curves), with fixed Cu:Al = 0.5 and Si:Al = 5, 15 and 29, respectively, after He-activation at 500 °C; left inset: background-subtracted pre-edge 1s → 3d peak; right inset: first derivative of the XANES spectra reported in the main panel in the rising-edge region. (b, c) Magnitude (b) and imaginary part (c) of the FT-EXAFS spectra for the He-activated samples reported in part (a), obtained by Fourier transforming the $k^2\chi(k)$ curves reported Figure S10c,d (SI) in the (2.4−10.8) Å^{-1} range. (d-f) XAS spectra for 0.5Cu-SSZ-13(5), 0.5Cu-SSZ-13(15) and 0.5Cu-SSZ-13(29) as parts (a-c) but collected after re-oxidation in O_2 at 500 °C of the He-activated samples.

Table 1. Fractions of framework-interacting Cu^{II} and Cu^{I} species evaluated by XANES LCF analysis for samples 0.5Cu-SSZ-13(5), 0.5Cu-SSZ-13(15) and 0.5Cu-SSZ-13(29) after He-activation together with correspondent LCF R-factors. Total fraction of Cu species at *1Al* sites is also reported, and compared with values extracted from the compositional phase diagram from ref. [47]

Sample (He Act. 500 °C)	LCF R-factor	Fraction of framework-interacting Cu-species				
		2Al Z_2Cu^{II}	*1Al* Z[Cu^{II}OH]	*1Al* ZCu^{I}	Total *1Al*[a]	Total *1Al*[b]
0.5Cu-SSZ-13(5)	$1 \cdot 10^{-4}$	0.51 ± 0.03	0.00 ± 0.02	0.47 ± 0.01	0.47 ± 0.03	~ 0.50
0.5Cu-SSZ-13(15)	$3 \cdot 10^{-4}$	0.08 ± 0.03	0.13 ± 0.03	0.79 ± 0.01	0.92 ± 0.04	~ 0.85
0.5Cu-SSZ-13(29)	$6 \cdot 10^{-4}$	0.01 ± 0.04	0.35 ± 0.04	0.64 ± 0.01	0.99 ± 0.05	~ 0.95

[a] This work.

[b] Values extracted from the compositional phase diagram reported by Paolucci et al. in ref. [47]

For an accurate quantification of the Cu-speciation, we have taken advantage of the results of our recent work,[64] where advanced multivariate curve resolution (MCR) methods were applied to extract the theoretical XANES signatures of 'pure' Cu-species formed in He-activated Cu-SSZ-13 as a function of the Si:Al ratio. These pure XANES curves, previously connected with well-defined local geometries of Cu-ions by multi-component EXAFS fits,[64] have been employed here as references to assess Cu-speciation from the spectra reported in Figure 5a by linear combination fit (LCF) analysis (see SI, Section 5.5 for additional details). As expected, Cu-speciation in the He-activated state at 500 °C is dominated by framework-interacting Cu-species, including *1Al* sites in their oxidized, Z[Cu^{II}OH], and reduced, ZCu^{I}, form as well as *2Al* Z_2Cu^{II} sites. The contributions from mobile Cu^{II} complexes are almost negligible (< 3% total Cu) for all samples. The fractions of framework-interacting Cu^{II} and Cu^{I} species evaluated by LCF analysis are reported in Table 1.

From Table 1 it is evident that for Si:Al = 5 a substantial contribution of redox-inert $2Al$ Z_2Cu^{II} sites is present (51% total Cu), as also reflected in the higher intensity of both first and second maximum in the corresponding FT-EXAFS spectrum with respect to the other He-activated samples (Figure 5b,c). The sample with Si:Al = 15 shows optimal reducibility: LCF reveals 79% of ZCu^I species and around 10% of both residual $Z[Cu^{II}OH]$ species and Z_2Cu^{II} sites in 6r. Concomitantly, the FT-EXAFS indicates a majority of twofold-coordinated sites, and a dampened/broadened second-shell peak, in relation with higher mobility of Cu^I cations and heterogeneity in ZCu^I siting.[64, 66] Finally, the sample with Si:Al = 29 shows intermediate reducibility, with 64% of ZCu^I and 35% of $Z[Cu^{II}OH]$ surviving in their oxidized state; at such low Al-loading, $2Al$ Z_2Cu^{II} are almost undetectable.

These findings fit well into the larger picture developed so far in the literature about the influence of composition on Cu-speciation in Cu-SSZ-13 materials prepared by solution ion exchange. As it can be also observed in Table 1, the total fractions of Cu-species hosted at $1Al$ sites determined here by XANES LCF analysis are in excellent agreement with the correspondent values extracted from the theoretical compositional phase diagram reported by Paolucci et al.[47] The presence of two Cu docking sites yielding Cu-species with markedly different redox properties also provides the basis to rationalize the two peaks observed during H$_2$-TPR experiments on Cu-SSZ-13 materials.[70] Focusing on the compositional impact, Gao et al. [70] systematically analyzed several Cu-SSZ-13 zeolites by TPR with Si:Al ratios of 6, 12 and 35, and Cu:Al ratios in the 0.005-0.44 range. Two reduction peaks at ~230 °C (~250 °C for the Si:Al = 35 samples) and at ~380 °C, are observed throughout the compositional series, assigned to reduction of partially hydrated Cu^{II} and $[Cu^{II}OH]^+$ ions within CHA cages, and of Cu^{II} hosted at $2Al$ sites in 6R. The trends observed in the intensity of the reduction peaks as a function of the composition corroborates that Cu^{II} ions at $2Al$ Z_2Cu^{II} sites possess a significantly higher binding energy to the CHA framework. TPR results also indicate that their fraction decreases by increasing either the Si:Al ratio or the Cu:Al ratio in the material, in line with the values reported in Table 1.

Figure 5d-f shows how re-oxidation in O$_2$ at 500 °C effectively restores a largely dominant Cu^{II} state, irrespectively of the composition. The characteristic XAS fingerprints of $2Al$ Z_2Cu^{II} sites[47, 64] remain a distinctive feature at Si:Al = 5, while the re-oxidized 0.5Cu-SSZ-13(29) and 0.5Cu-SSZ-13(15) samples show a very similar XANES. However, we observe significant differences in the FT-EXAFS at Si:Al = 15 and 29. In particular, at Si:Al = 29, a lower first-shell peak is observed, together with an overall deterioration of the EXAFS signal, connected with a higher heterogeneity in the Cu^{II} component. The absence of a well-defined third maximum in the FT-EXAFS at Si:Al = 29 suggest that the formation of multinuclear oxo or peroxo Cu^{II} species is hampered in this sample. The development of such EXAFS feature appears to be inversely correlated with the Si:Al ratio (see SI, Figure S11), in line with the statistical availability of suitable docking sites with Al-Al separation < 10 Å[71-72]

Correlating the LCF results reported in Table 1 with the performance of the investigated Cu-zeolites with Si:Al = 5, 15, 29, we found a linear correlation between the normalized productivity and the sample reducibility in the He-activated state, quantified through the fraction of ZCu^I. The productivity-reducibility correlation is highlighted in Figure 6, demonstrating that the normalized methanol productivity is directly proportional to the relative abundance of Cu^I sites available for high-temperature reaction with O$_2$ to a set of $Cu^{II}_xO_y$ species among which the active sites should be searched. Thereby, it is also clear that redox-inert $2Al$ Z_2Cu^{II} site are inactive toward the conversion of methane. Although our recent study[64] suggests that a complete '$2Al$ saturation' scenario is unlikely, there is solid evidence in the literature that points towards a preferential population of $2Al$ sites at low Cu-loading.[47, 70, 73] We can therefore also link the lower normalized productivity observed in low-loading Cu-SSZ-13 samples (Cu:Al ~ 0.15) at Si:Al = 12 (see

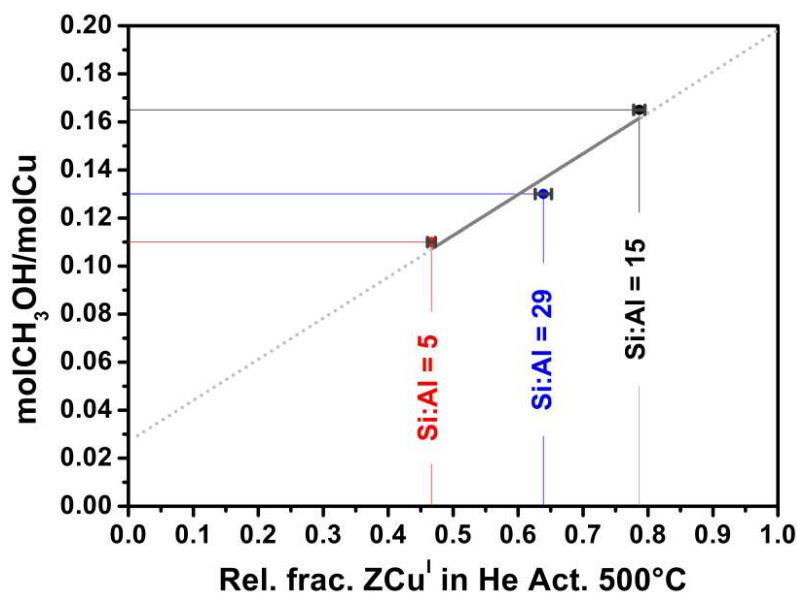Figure 4a) with a higher relative abundance of Z_2Cu^{II} species.

Figure 6. Correlation between the normalized productivity of Cu-SSZ-13 samples with Si:Al = 5, 15, 29 and their reducibility in the He-activated state, quantified through the relative fraction on ZCu^I from LCF of the XANES spectra reported in Figure 5a. The best fit line through the experimental points is reported in grey.

So far, we have not answered the question about the nuclearity of $Cu^{II}_xO_y$ species derived from the re-oxidation of ZCu^I, and whether the nuclearity correlates with productivity in Cu-SSZ-13. Unfortunately, the EXAFS signature of such species is only found in the high-R range, where the technique sensitivity inherently decreases (especially for high-temperature measurements on complex, multi-component systems). Moreover, Cu-Cu contributions prevail over the more abundant Cu-O ones only in high k-range, where the increased noise could significantly affect the FT-EXAFS signal. To further assess this aspect, we thus employed Raman spectroscopy as a complementary technique in order to identify fingerprints correlated to multimeric $Cu^{II}_xO_y$ species, as described in Section 2.5.

2.5 Complementary Results from Raman and FTIR and Spectroscopy

Raman spectroscopy is a highly sensitive technique to detect the presence of multinuclear $Cu^{II}_xO_y$ species in zeolites, due to the fact that resonance conditions towards these moieties can be achieved by proper excitation.[25, 60, 74] The Raman spectrum of the O_2 activated 0.5Cu-SSZ-13(15) sample (Figure 7a, red line) shows a series of new bands which are absent in the hydrated sample (Figure 7a, black line), revealing the presence of several oxygen-activated Cu^{II} species.

The bands at 510, 580 and 830 cm^{-1} were also observed by Ipek et.al[25] for activated Cu-SSZ-13 and assigned to $[Cu(trans-\mu-1,2-O_2)Cu]^{2+}$ species. In addition, we observe strong Raman bands between ~1000-1200 cm^{-1} (exhibiting maxima at 1100 and 1155 cm^{-1}) for the activated sample, in agreement with the presence of $[Cu^{II}O_2^\bullet]^+$ superoxo species.[74] The broadness of the bands, suggests that the Cu-superoxo species are located at various Cu sites, as well as in different coordination symmetries (end-on vs side-on).[75-76] The presence of $[Cu-(\mu-O)-Cu]^{2+}$ species is not easy to access, due to the very intense band at 580 cm^{-1}, which is the range where one would expect the symmetric metal-oxo stretch of such species.[25] However, a shoulder at ~620 cm^{-1} adumbrates their presence. In this context, Ipek et.al observed a fast intensity decrease of the band at 580 cm^{-1} with time, which they ascribed to small amounts of water leaking into the system and the high sensitivity of the $[Cu(trans-\mu-1,2-O_2)Cu]^{2+}$ species towards hydrolysis. Interestingly, we found $[Cu(trans-\mu-1,2-O_2)Cu]^{2+}$ to be sensitive to the measurements conditions, such as different sampling times and laser powers (Figure 7b). By increasing the energy at the sample through higher laser power and/or longer sampling time the intensity of the 580 cm^{-1} band increases. At very low laser power (~0.1 mW, Figure 7b, purple line) or at short exposure at ~1 mW (Figure 7b, pink line), the latter is diminished significantly whereas a band at 620 cm^{-1} (assigned to the $[Cu-(\mu-O)-Cu]^{2+}$ species) [25] becomes visible. In the case of the spectrum of the activated sample (Figure 7a, red line), we aimed for a high-quality spectrum and therefore applied a sampling time of 120 min at laser output power of ~1mW. The high energy input therefore explains the high intensity of the band at 580 cm^{-1}, overshadowing the much weaker band at 620 cm^{-1} (observed as a shoulder in this case).

Since the samples were sealed in capillaries at ~550 °C (see SI, Section 1.5), we can exclude a hydration-related effect as suggested by Ipek et.al. [25] We suspect in our case a temperature-related effect, due to laser heating, as the cause for the observed changes in the spectrum. However, such behavior requires a careful evaluation and will be the object of future investigation.
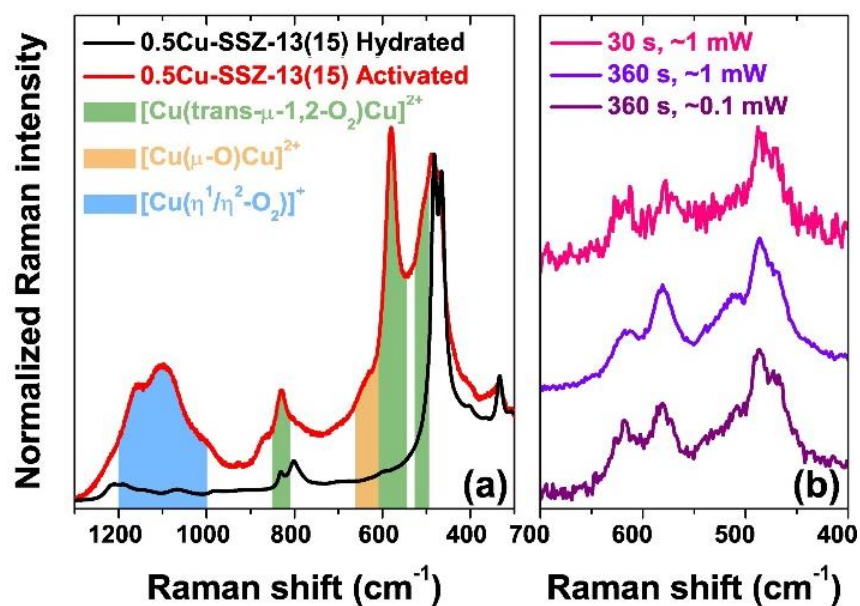

Figure 7. (a) Raman spectra of 0.5Cu-SSZ-13(15) in its hydrated (black line) and activated (red line) forms. The spectral contributions from the observed $Cu^{II}_xO_y$ moieties are highlighted: $[Cu(trans-\mu-1,2-O_2)Cu]^{2+}$ (green filling); $[Cu-(\mu-O)-Cu]^{2+}$ (orange filling); and $[Cu^{I-I}O_2^\bullet]^+$ (light-blue filling). (b) Raman spectra of the activated sample, collected at different exposure times and excitation laser powers. The spectra on activated 0.5Cu-SSZ-13(15) have been collected with the sample inside sealed capillaries (see SI, section 1.5). All the spectra have been normalized to the most intense feature of the SSZ-13 framework (485 cm^{-1}) and vertically shifted for sake of visualization.

To further complement the characterization of relevant Cu-species for the conversion of methane to methanol, we chose Infrared (IR) spectroscopy, to monitor the O_2-activation step to 400 °C. In the 3800 to 3500 cm^{-1} range, the spectra exhibit common features related to ν(O-H) modes of silanols at (3737 cm^{-1}) as well as Brønsted sites at 3611 cm^{-1} and 3584 cm^{-1}.[40-41] Another distinct band around 3650 cm^{-1} gradually decreases as the temperature increases. In previous studies, such band has been identified as the finger-

print of [Cu^{II}OH]$^+$ species in Cu-SSZ-13.[40] The spectrum collected at 400 °C shows a clear depletion in intensity of the specific feature which decreases further after 150 mins at that temperature. As discussed in the previous sections, such species are unlikely to be the active species for the methane activation. However, the data confirms that high temperature combined with prolonged exposure time in oxidative atmosphere depletes the population of [Cu^{II}OH]$^+$ sites. This trend is in agreement with the picture obtained from XAS and Raman spectroscopy, indicating that during O$_2$ activation at high temperature [Cu^{II}OH]$^+$ species further evolve, acting as precursors for new species, most probably the active sites, as will be discussed in the following section.
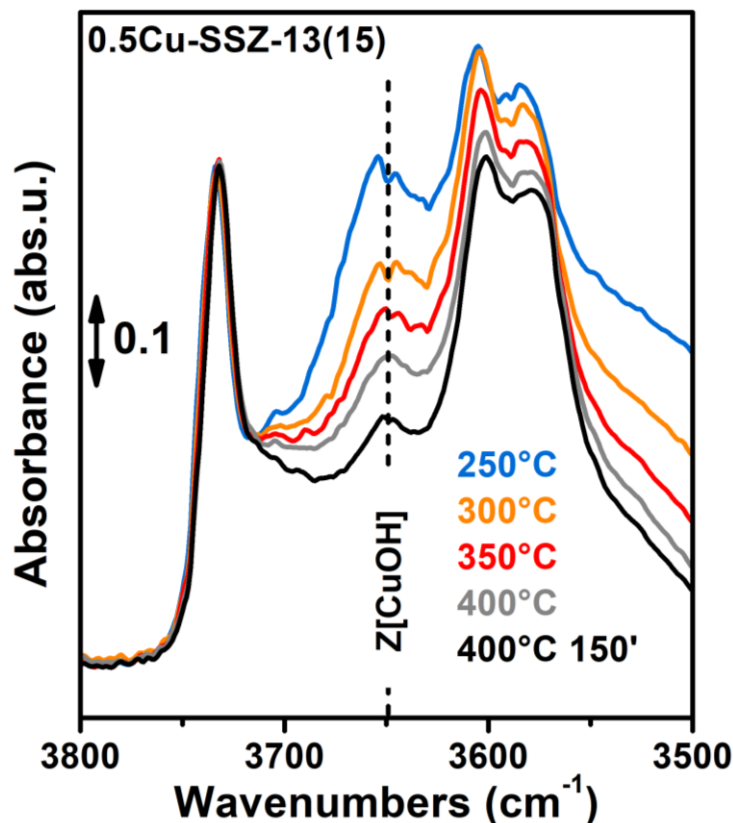

Figure 8. O$_2$ activation of sample 0.5Cu-SSZ-13(15) monitored by in situ FTIR spectroscopy in the 250–400°C range, in the ν(OH) region. The dotted line highlights the progressive decrease in the intensity of the band at ca. 3650 cm^{-1} (fingerprinting Z[Cu^{II}OH]) as temperature increases.

3. THE FORMATION OF ACTIVE CU SPECIES

We have shown that the availability of Cu^{I} sites able to react with O$_2$ at high temperature has a key impact on the methanol productivity. The reducibility of Cu-SSZ-13, and, in general, the resulting Cu speciation, is highly dependent on the composition, in terms of Si:Al and Cu:Al ratios. Optimal methanol productivity is associated with optimal reducibility, so that the compositional characteristics of the material have to be tuned in order to maximize the relative fraction of Cu sites efficiently undergoing self-reduction during activation. As depicted in Scheme 1a and further corroborated by a number of previous studies,[40, 42, 45, 47, 64, 69-70, 73, 77] this condition is met at intermediate Si:Al ratios (~ 12−15) and high Cu-loading (~ 0.5). Instead, low Si:Al and low Cu-loading promote large populations of redox-inert *2Al* Z$_2$Cu^{II}, trapping Cu sites in stable, inactive positions in the *6r*. However, when the Si:Al ratio increases beyond the optimum (~ 30), although the relative fraction of *1Al* sites is maximized, the redox potential of such species is diminished, suggesting that the efficiency of the self-reduction process depends on the Brønsted acid site density in the material. Z[Cu^{II}OH] complexes at *1Al* sites efficiently undergoing self-reduction (middle panel in Scheme 1a) are thus identified as the precursors to the active sites responsible for the methane to methanol conversion in Cu-SSZ-13.

In Scheme 1b we give an overview of the possible routes for the formation of active Cu$^{II}_x$O$_y$ species, which we will critically discuss by combining the results presented in the previous sections with key findings from literature. Complementary, Table 2 reports a selection of spectroscopic fingerprints for the Cu-species presented in Scheme 1b. It is worth to note that Scheme 1b only considers Cu^{I} and Cu^{II} species, since the formation and the involvement of Cu^{III} moieties, e.g. bis(μ-oxo) dicopper(III), have been ruled out based on the absence of any Cu^{III} evidence either from XAS[60,78] and from Raman[79] in all the experimental conditions monitored in the present study.

The homolytic cleavage of the Cu−OH bond in the Z[Cu^{II}OH] precursor (**1** in Scheme 1b), yielding a reduced ZCu^{I} site (**2**) and an HO$^{•}$ radical is envisaged as an initial key step towards the active species formation. Temperature-dependent IR data (Figure 8) evidence that this step is also occurring to some extent in O$_2$ flux. The methane-converting Cu$^{II}_x$O$_y$ species can be primarily formed by direct reaction between O$_2$ and the available ZCu^{I} sites (Scheme 1b, top part). This is supported by our observation that introduction of O$_2$ after He-activation at 500 °C promptly restores a largely dominant Cu^{II} state rather irrespectively of the tested re-

oxidation temperature: ~ 90% total Cu is found as Cu^{II} both carrying out the re-oxidation at 500 and at 200 °C. Starting from isolated ZCu^I sites, Cu^{II} moieties possibly formed under these conditions include $ZCu^{II}O_2^{\bullet}$ superoxo complexes, with either end-on $Cu(\eta^1\text{-}O_2)$ or side on $Cu(\eta^2\text{-}O_2)$ binding modes, species (**3a**) and (**3b**), respectively. Multimeric peroxo-Cu^{II} species such as $ZCu^{II}(O_2)Cu^{II}Z$ (**4**) can be also formed. The probability to stabilize such multimeric moieties depends on the proximity of Al atoms in the zeolite framework: Al−Al separations up to ~10 Å are envisaged to enable suitable docking sites for neighboring Cu ions. As may be observed in Scheme 1b, having two ZCu^I satisfying the aforementioned criterion, it is possible that they react with O_2 to $ZCu^{II}(O_2)Cu^{II}Z$ species, e.g. forming $[Cu(trans\text{-}\mu\text{-}1,2\text{-}O_2)Cu]^{2+}$ (**4a**) or $[Cu(\mu\text{-}\eta^2\text{:}\eta^2\text{-}O_2)Cu]^{2+}$ complexes (**4b**).

Indeed, EXAFS analysis supports the formation of multinuclear Cu^{II} species in Cu-SSZ-13 with average Cu-Cu distances of ~ 3.4 Å, involving ca. 30% of Cu sites in the O_2-activated material. As summarized in Table 2, with Raman we were able to identify the spectroscopic fingerprints of both $ZCu^{II}O_2^{\bullet}$ superoxo complexes in different coordination modes (**3**) and of $[Cu(trans\text{-}\mu\text{-}1,2\text{-}O_2)Cu]^{2+}$ (**4a**). Conversely, species **4b** was previously identified in Cu-ZSM-5,[81] but has not been detected by Raman neither by us nor in the recent study by Ipek et al.[25]

Importantly, the average coordination mode, side-on- or end-on-like, in such species is found to be influenced by the operation temperature. As discussed in Section 2.3, cooling down to methane loading temperature (i.e. 200 °C) during *operando* XAS experiments, we observe modifications in both XANES and FT-EXAFS spectra pointing to an increased coordination number in the Cu-O_{ef} shell at lower temperature. The XAS data are consistent with a partial temperature-induced transition from end-on to side-on O_2 binding modes, resulting in threefold and fourfold coordinated Cu^{II}-sites, respectively. We observe the same spectroscopic fingerprints, but more pronounced, after re-oxidation of the pre-reduced sample at 200 °C, which also leads to a significantly lower methanol yield compared to re-oxidation at 500 °C. These observations suggest that a tridentate framework-interacting Cu^{II} site with end-on binding mode of an O_2-derived ligand, as it seen e.g. in species **3a**, **4a** or **6**, represents the most favorable site geometry for methane conversion.

Apart from the formation of Cu_xO_y species through the reaction of O_2 with Cu^I sites, internal pathways have also been proposed in the literature, based on experimental evidences and theoretical studies[25, 31, 35, 62-63, 82] (Scheme 1b, bottom part). Such pathways explain the residual productivity observed after pre-treatment in inert. If the OH$^{\bullet}$ released during the self-reduction of a first $Z[Cu^{II}OH]$ is able to reach another $Z[Cu^{II}OH]$ complex, a $ZCu^{II}O^{\bullet}$ (**5**) could be formed together with an H_2O molecule.[35, 62-63] Albeit species (**5**) has been previously indicated as one of the most effective in methane activation,[34, 83-84] to the best of our knowledge this highly reactive intermediate has never been detected in Cu-zeolites, hence its existence and role remain speculative.

DFT studies actually support the self-organization of mononuclear oxygenated/hydroxylated cations in zeolite frameworks towards oxygen-bridged binuclear complexes (black dashed arrows in Scheme 1b). Computational analysis predicts energetic benefits as high as 400 kJ mol^{-1} associated with such self-organization phenomena, in connection with the stabilization of under-coordinated metal centers with excessively basic terminal O/OH ligands.[82] Interestingly, tridentate $ZCu^{II}O^{\bullet}$ complexes in Cu-MFI are predicted to dimerize into either bis(μ-oxo)-dicopper or μ-$(\eta^2\text{:}\eta^2)$-peroxo dicopper cores for two different docking sites with Al−Al separations of 5.48 and 8.72 Å, respectively.[82] Similarly, condensation of two $Z[Cu^{II}OH]$ complexes at a suitable distance will result in the formation of a H_2O molecule and a mono-(μ-oxo) dicopper core (**6** in Scheme 1b), currently indicated as the active site for direct methanol conversion in Cu-ZSM-5 and Cu-MOR[6, 31-32, 34, 74] High-temperature treatment in O_2-deficent atmosphere has been proposed to favour desorption of the bridging oxygen from the oxocationic species,[81, 85] leaving two Cu(I) sites and an O_{ef} vacancy. In this context, Smeets *et al.*[81] demonstrated that first a μ-$(\eta^2\text{:}\eta^2)$-peroxo dicopper species is formed by reacting O_2 at RT with a pre-reduced Cu-ZSM-5 zeolite, which is then transformed into mono-(μ-oxo) dicopper upon thermally-driven oxygen elimination from 175 °C upwards (orange dashed orange arrow in Scheme 1b). Our Raman data indicate that the mono-(μ-oxo) dicopper core (**6**) is also present in air-activated Cu-SSZ-13, as seen in Figure 7 and shown by Ipek et.al.[25] Beside bis-μ-oxo dicopper species, Cu-trimers have been also proposed to form in O_2-activated Cu-MOR.[12] Moreover, from DFT, clusters of even higher nuclearity have been suggested as favorable sites for the methane conversion.[33-34] Nonetheless, combining our XAS and Raman results on Cu-SSZ-13, no evidence for Cu_xO_y species with x > 2 is obtained.

13
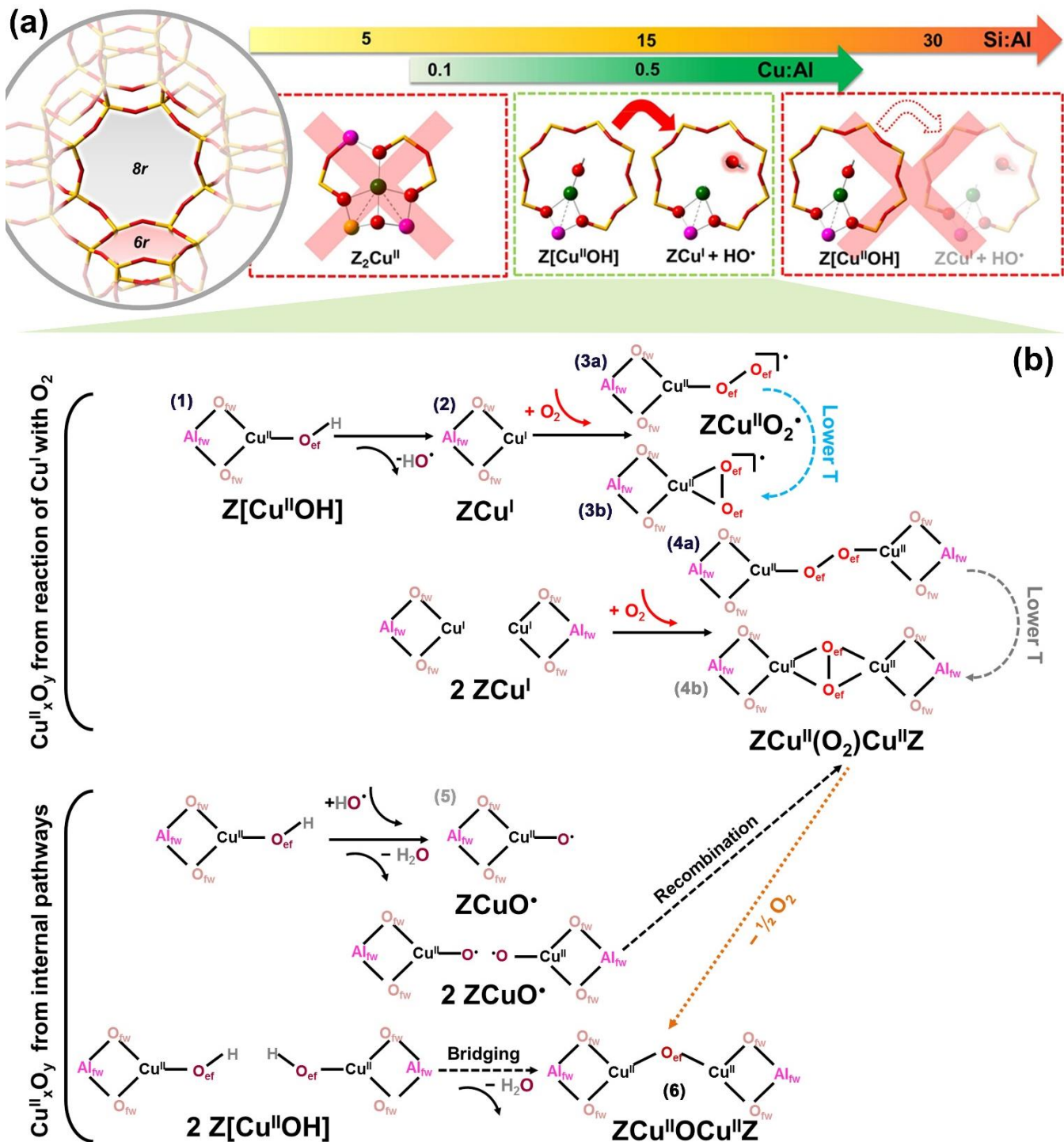
Scheme 1. (a) Rationalization of the effect of composition (Cu:Al and Si:Al ratios) on the productivity for the methane to methanol conversion over Cu-SSZ-13. (b) Possible mechanisms for the formation of active $Cu^{II}_xO_y$ moieties from precursor *1Al* $Z[Cu^{II}OH]$ sites, considering $Cu^{II}_xO_y$ formation from reaction of self-reduced ZCu^I sites with O_2 (top part) and from internal pathways (bottom part). Selected spectroscopic fingerprints for the Cu-species (1)-(6) presented in the scheme, are summarized in Table 2, comparing previous literature and experimental observations in the present work. Species indicated with grey labels have been previously detected in Cu-zeolites (4b) or proposed as intermediates (5) but are not directly observed in this study on Cu-SSZ-13 materials.

14

Table 2. Selected spectroscopic fingerprints for the Cu species presented in Scheme 1, derived from previous literature on Cu-zeolites and/or Cu model compounds and experimental data reported in the present work. FTIR frequencies and Raman shifts are reported in cm^{-1}.

Cu species in Scheme 1		Relevant FTIR, Raman and XAS spectroscopic fingerprints	
		Previous literature [ref.]	This work
(**1**) Z[Cu^{II}OH]		FTIR: ν(O-H) ~ 3650 [40-41, 47] XAS: Cu^{II}, 3C [40-41, 47]	FTIR: ν(O-H) 3650 XAS: Cu^{II}, 3C^a
(**2**) ZCu^{I}		N$_2$-FTIR: ZCu^I-N$_2$ 2300, 2992 [64, 67] CO-FTIR: ZCu^I(CO) 2155; ZCu^I(CO)$_2$ 2178, 2148; ZCu^I(CO)$_3$ 2194, 2169 (sh), 2134 (sh) [67] XAS: Cu^I, 2C [40, 47, 64]	XAS: Cu^I, 2C
(**3**) ZCu^{II}O$_2$$^{\bullet}$	(**3a**) [Cu(η^1-O$_2$)]$^+$	Raman: ν(O-O) 1121, ν(Cu-O) 472 [74-75]	Raman: ν(O-O) broad bands with maxima at 1100 and 1155 XAS: Cu^{II} 3C/4C
	(**3b**) [Cu(η^2-O$_2$)]$^+$	Raman: ν(O-O) 1043, ν(Cu-O) 554 [74, 76]	
(**4**) ZCu^{II}(O$_2$)Cu^{II}Z	(**4a**)[Cu(trans-μ-1,2-O$_2$)Cu]$^{2+}$	Raman: ν(O-O) 837, ν(Cu-O) 510, 580 [25]; ν(O-O) 832, ν(Cu-O) 561 [25, 80]	Raman: ν(O-O) 830, ν(Cu-O) 507, 580 (laser-sensitive)
	(**4b**) [Cu(μ-η^2:η^2-O$_2$)Cu]$^{2+}$	Raman: ν(O-O) 736, ν(Cu-O) 269 [81]; ν(O-O) 763, ν(Cu-O) 284 [80]; Not observed in [25]	Raman: Not observed
(**5**) ZCu^{II}O$^{\bullet}$		Not identified	Not identified
(**6**) ZCu^{II}OCu^{II}Z	(**6**) [Cu-(μ-O)-Cu]$^{2+}$	Raman: ν(Cu-O) 616-617 [25]; XAS: Cu^{II} 3C; Cu−Cu ~ 2.9 Å in Cu-MOR [31] and Cu-ZSM-5 [57]	Raman: ν(Cu-O) 618 XAS: Cu^{II} 3C; Cu−Cu 3.42 Å

Note: for species (**4**), This work column also reports: XAS: Cu^{II} 3C/4C; Cu−Cu 3.42 Å

^{a} 2C, 3C,4C = 2-, 3-, 4-fold coordinated Cu species with O$_{ef}$ and O$_{fw}$ atoms the first coordination sphere, respectively.

Based on these considerations, the residual Cu^{II} component observed after He-activation of Cu-SSZ-13 with Si:Al in the 12-15 range could be ascribed to a mixture of inactive Z$_2$Cu^{II} sites in *6r* and active ZCu^{II}OCu^{II}Z cores still retaining their oxo bridge, which would account for the corresponding non-zero yield. These internal pathways to Cu$^{II}_x$O$_y$ moieties can, in principle, occur also during O$_2$-activation in parallel to reactions of newly formed Cu^I sites. In this case, the O$_2$-rich atmosphere is expected to limit the aforementioned oxygen desorption phenomena, thus enriching the population of ZCu^{II}OCu^{II}Z cores. In Cu-SSZ-13, these latter species have so far been assumed only to form in *8r* containing 2 Al atoms, corresponding to DFT-optimized Cu-Cu distances in the 2.6-3.1 Å range, depending on the number of Si atoms separating the two Al sites.[36, 72] The longer Cu-Cu distances found here by EXAFS, more similar to what predicted for mono-(μ-oxo) dicopper in the *12r* of Cu-MOR (Cu-Cu ~ 3.5 Å[72]) could suggest these species to form also by bridging two Cu centers distinctly located in *8r* and *6r*, as previously found from DFT for a ZCu^{II}O$_2$Cu^{II}Z complex.[25, 71]

Summarizing Scheme 1, Z[Cu^{II}OH] precursors can evolve to a set of tri-coordinated Cu^{II} moieties either from direct reaction of self-reduced ZCu^I with O$_2$, giving [Cu(η^1-O$_2$)]$^+$ superoxo or [Cu(trans-μ-1,2-O$_2$)Cu]$^{2+}$ peroxo complexes, or from internal pathways, resulting e.g. in mono-(μ-oxo) dicopper cores. The abundance of multi-copper species is definitely determined by the availability and distribution of Al in the zeolite.

4. CONCLUSIONS

The individual process steps in the direct conversion of methane to methanol over Cu-SSZ-13 materials have been investigated in detail and relationships between productivity and Cu-speciation have been established. High-temperature treatment at 500 °C in oxygen and a prolonged activation time positively impact the productivity, as a result of an increased formation of reactive Cu^{II} species. We evidence how high partial pressure of CH$_4$ at 200 °C is required to achieve saturation of the active centers with reactive intermediates, and illustrate the possibility of isothermal extraction of methanol. Employing optimized process conditions, we are able to achieve a methanol productivity equal of 0.172 molCH$_3$OH/molCu (107 µmol/g). Intriguingly, four cycles of the process drive the productivity to 0.202 molCH$_3$OH/molCu (125 µmol/g). This increase is related to the water-assisted mobilization of the metal centers during the extraction step, driving higher fractions of Cu into the active framework positions.

Our results support tri-coordinated framework-interacting Cu^{II} centers, with two O$_{fw}$ and one O$_{ef}$ ligands in the first metal coordination sphere, as the most favorable sites for methane conversion. We found this coordination mode to be dominant at 500 °C, whereas at 200 °C four-coordinated Cu^{II} species appear to be also present, resulting in a lower productivity. By coupling the XAS spectroscopic insights with the results from activity measurements, we were able to exclude the direct involvement of Z[Cu^{II}OH]

complexes. These species progressively deplete during exposure to high temperature oxidative treatment, and are proposed to be precursor to the active species.

Via *operando* XAS we directly probed the Cu^{II} to Cu^{I} reduction of 27% of the Cu sites during methane loading. However, a certain fraction of the Cu^{I} formed during interaction with methane likely originates from pathways leading to over-oxidation products. Indeed, during H_2O-assisted extraction, we observed the re-oxidation of only about half of the previously reduced Cu sites (13% total Cu), identified as the actual reactive sites.

Furthermore, we explored the correlations between elemental composition (Cu:Al and Si:Al ratios) in Cu-SSZ-13 and methanol productivity. The combination of testing and XAS measurements clearly evidences a positive linear correlation between the methanol productivity and the reducibility of the Cu centers. The high redox inertness of *2Al* Z_2Cu^{II} sites in *6r*, favored at low Si:Al and low Cu-loading, results in completely inactive Cu sites for the methane to methanol conversion. Instead, intermediate Si:Al ratios (~ 12−15) and high Cu-loading (~ 0.5) lead to a high population of $Z[Cu^{II}OH]$ sites, ultimately resulting in high methanol yields per Cu.

ASSOCIATED CONTENT

The Supporting Information is available free of charge via the Internet at http://pubs.acs.org. Material Synthesis; Laboratory Characterization; Experimental Details; XAS Analysis; Linear Combination Fitting;

AUTHOR INFORMATION

Corresponding Authors

* Elisa Borfecchia: **elisa.borfecchia@unito.it**

* Stian Svelle: **stian.svelle@kjemi.uio.no**

* Pablo Beato: **pabb@topsoe.com**

ACKNOWLEDGMENT

REFERENCES

1. Gesser, H. D.; Hunter, N. R.; Prakash, C. B., *Chem. Rev.* **1985,** *85*, 235-244.
2. Lunsford, J. H., *Cat. Today* **2000,** *63*, 165-174.
3. Saha, D.; Grappe, H. A.; Chakraborty, A.; Orkoulas, G., *Chem. Rev.* **2016,** *116*, 11436-11499.
4. Horn, R.; Schlögl, R., *Catal. Lett.* **2015,** *145*, 23-39.
5. da Silva, M. J., *Fuel Process. Technol.* **2016,** *145*, 42-61.
6. Sushkevich, V. L.; Palagin, D.; Ranocchiari, M.; van Bokhoven, J. A., *Science* **2017,** *356*, 523-527.
7. Tomkins, P.; Mansouri, A.; Bozbag, S. E.; Krumeich, F.; Park, M. B.; Alayon, E. M.; Ranocchiari, M.; van Bokhoven, J. A., *Angew. Chem. Int. Ed.* **2016,** *55*, 5467-71.
8. Lieberman, R. L.; Rosenzweig, A. C., *Nature* **2005,** *434*, 177-182.
9. Balasubramanian, R.; Smith, S. M.; Rawat, S.; Yatsunyk, L. A.; Stemmler, T. L.; Rosenzweig, A. C., *Nature* **2010,** *465*, 115-9.
10. Tinberg, C. E.; Lippard, S. J., *Acc. Chem. Res.* **2011,** *44*, 280-8.
11. Groothaert, M. H.; Smeets, P. J.; Sels, B. F.; Jacobs, P. A.; Schoonheydt, R. A., *J. Am. Chem. Soc.* **2005,** *127*, 1394-1395.
12. Grundner, S.; Markovits, M. A.; Li, G.; Tromp, M.; Pidko, E. A.; Hensen, E. J.; Jentys, A.; Sanchez-Sanchez, M.; Lercher, J. A., *Nat. Commun.* **2015,** *6*, 7546.
13. Alayon, E. M. C.; Nachtegaal, M.; Kleymenov, E.; van Bokhoven, J. A., *Microporous Mesoporous Mater.* **2013,** *166*, 131-136.
14. Beznis, N. V.; Weckhuysen, B. M.; Bitter, J. H., *Catal. Lett.* **2010,** *138*, 14-22.
15. Wulfers, M. J.; Teketel, S.; Ipek, B.; Lobo, R. F., *Chem. Commun.* **2015,** *51*, 4447-4450.
16. Kalamaras, C.; Palomas, D.; Bos, R.; Horton, A.; Crimmin, M.; Hellgardt, K., *Catal. Lett.* **2016,** *146*, 483-492.
17. Hammond, C.; Forde, M. M.; Ab Rahim, M. H.; Thetford, A.; He, Q.; Jenkins, R. L.; Dimitratos, N.; Lopez-Sanchez, J. A.; Dummer, N. F.; Murphy, D. M.; Carley, A. F.; Taylor, S. H.; Willock, D. J.; Stangland, E. E.; Kang, J.; Hagen, H.; Kiely, C. J.; Hutchings, G. J., *Angew. Chem. Int. Ed.* **2012,** *51*, 5129-33.
18. Shan, J.; Huang, W.; Nguyen, L.; Yu, Y.; Zhang, S.; Li, Y.; Frenkel, A. I.; Tao, F. F., *Langmuir* **2014,** *30*, 8558-69.
19. Krisnandi, Y. K.; Putra, B. A. P.; Bahtiar, M.; Zahara; Abdullah, I.; Howe, R. F., *Procedia Chem.* **2015,** *14*, 508-515.
20. Bozbag, S. E.; Alayon, E. M. C.; Pecháček, J.; Nachtegaal, M.; Ranocchiari, M.; van Bokhoven, J. A., *Catal. Sci. Technol.* **2016,** *6*, 5011-5022.
21. Alayon, E. M.; Nachtegaal, M.; Ranocchiari, M.; van Bokhoven, J. A., *Chem. Commun.* **2012,** *48*, 404-6.
22. Grundner, S.; Luo, W.; Sanchez-Sanchez, M.; Lercher, J. A., *Chem. Commun.* **2016,** *52*, 2553-6.
23. Narsimhan, K.; Iyoki, K.; Dinh, K.; Roman-Leshkov, Y., *ACS Cent. Sci.* **2016,** *2*, 424-9.
24. Ipek, B.; Lobo, R. F., *Chem. Commun.* **2016,** *52*, 13401-13404.
25. Ipek, B.; Wulfers, M. J.; Kim, H.; Göltl, F.; Hermans, I.; Smith, J. P.; Booksh, K. S.; Brown, C. M.; Lobo, R. F., *ACS Catal.* **2017,** *7*, 4291-4303.
26. Sheppard, T.; Daly, H.; Goguet, A.; Thompson, J. M., *ChemCatChem* **2016,** *8*, 562-570.
27. Xu, J.; Armstrong, R. D.; Shaw, G.; Dummer, N. F.; Freakley, S. J.; Taylor, S. H.; Hutchings, G. J., *Cat. Today* **2016,** *270*, 93-100.
28. Tsai, M.-L.; Hadt, R. G.; Vanelderen, P.; Sels, B. F.; Schoonheydt, R. A.; Solomon, E. I., *J. Am. Chem. Soc.* **2014,** *136*, 3522-3529.
29. Sheppard, T.; Hamill, C. D.; Goguet, A.; Rooney, D. W.; Thompson, J. M., *Chem. Commun.* **2014,** *50*, 11053-5.
30. Le, H. V.; Parishan, S.; Saaltchik, A.; Gobel, C.; Schlesiger, C.; Malzer, W.; Trunschke, A.; Schomacker, R.; Thomas, A., *ACS Catal.* **2017,** *7*, 1403-1412.
31. Alayon, E. M.; Nachtegaal, M.; Bodi, A.; Ranocchiari, M.; van Bokhoven, J. A., *Phys Chem Chem Phys* **2015,** *17*, 7681-93.

32. Alayon, E. M. C.; Nachtegaal, M.; Bodi, A.; van Bokhoven, J. A., *ACS Catal.* **2014,** *4*, 16-22.

33. Palagin, D.; Knorpp, A. J.; Pinar, A. B.; Ranocchiari, M.; van Bokhoven, J. A., *Nanoscale* **2017,** *9*, 1144-1153.

34. Tomkins, P.; Ranocchiari, M.; van Bokhoven, J. A., *Acc. Chem. Res.* **2017,** *50*, 418-425.

35. Kulkarni, A. R.; Zhao, Z.-J.; Siahrostami, S.; Nørskov, J. K.; Studt, F., *ACS Catal.* **2016,** *6*, 6531-6536.

36. Mahyuddin, M. H.; Staykov, A.; Shiota, Y.; Miyanishi, M.; Yoshizawa, K., *ACS Catal.* **2017**, 3741-3751.

37. Brandenberger, S.; Krocher, O.; Tissler, A.; Althoff, R., *Catal. Rev.* **2008,** *50*, 492-531.

38. Deka, U.; Lezcano-Gonzalez, I.; Weckhuysen, B. M.; Beale, A. M., *ACS Catal.* **2013,** *3*, 413-427.

39. Beale, A. M.; Gao, F.; Lezcano-Gonzalez, I.; Peden, C. H. F.; Szanyi, J., *Chem. Soc. Rev.* **2015,** *44*, 7371-7405.

40. Borfecchia, E.; Lomachenko, K. A.; Giordanino, F.; Falsig, H.; Beato, P.; Soldatov, A. V.; Bordiga, S.; Lamberti, C., *Chem. Sci.* **2015,** *6*, 548-563.

41. Giordanino, F.; Borfecchia, E.; Lomachenko, K. A.; Lazzarini, A.; Agostini, G.; Gallo, E.; Soldatov, A. V.; Beato, P.; Bordiga, S.; Lamberti, C., *J. Phys. Chem. Lett.* **2014,** *5*, 1552-9.

42. Gao, F.; Walter, E. D.; Karp, E. M.; Luo, J.; Tonkyn, R. G.; Kwak, J. H.; Szanyi, J.; Peden, C. H. F., *J. Catal.* **2013,** *300*, 20-29.

43. Janssens, T. V. W.; Falsig, H.; Lundegaard, L. F.; Vennestrøm, P. N. R.; Rasmussen, S. B.; Moses, P. G.; Giordanino, F.; Borfecchia, E.; Lomachenko, K. A.; Lamberti, C.; Bordiga, S.; Godiksen, A.; Mossin, S.; Beato, P., *ACS Catal.* **2015,** *5*, 2832-2845.

44. Tyrsted, C.; Borfecchia, E.; Berlier, G.; Lomachenko, K. A.; Lamberti, C.; Bordiga, S.; Vennestrøm, P. N. R.; Janssens, T. V. W.; Falsig, H.; Beato, P.; Puig-Molina, A., *Catal. Sci. Technol.* **2016,** *6*, 8314-8324.

45. Lomachenko, K. A.; Borfecchia, E.; Negri, C.; Berlier, G.; Lamberti, C.; Beato, P.; Falsig, H.; Bordiga, S., *J. Am. Chem. Soc.* **2016,** *138*, 12025-8.

46. Godiksen, A.; Vennestrøm, P. N. R.; Rasmussen, S. B.; Mossin, S., *Top. Catal.* **2016,** *60*, 13-29.

47. Paolucci, C.; Parekh, A. A.; Khurana, I.; Di Iorio, J. R.; Li, H.; Albarracin Caballero, J. D.; Shih, A. J.; Anggara, T.; Delgass, W. N.; Miller, J. T.; Ribeiro, F. H.; Gounder, R.; Schneider, W. F., *J Am Chem Soc* **2016,** *138*, 6028-48.

48. Paolucci, C.; Verma, A. A.; Bates, S. A.; Kispersky, V. F.; Miller, J. T.; Gounder, R.; Delgass, W. N.; Ribeiro, F. H.; Schneider, W. F., *Angew. Chem. Int. Ed.* **2014,** *53*, 11828-33.

49. Bordiga, S.; Groppo, E.; Agostini, G.; van Bokhoven, J. A.; Lamberti, C., *Chem. Rev.* **2013,** *113*, 1736-1850.

50. Mathon, O.; Beteva, A.; Borrel, J.; Bugnazet, D.; Gatla, S.; Hino, R.; Kantor, I.; Mairs, T.; Munoz, M.; Pasternak, S.; Perrin, F.; Pascarelli, S., *J. Synchrot. Radiat.* **2015,** *22*, 1548-1554.

51. Nikitenko, S.; Beale, A. M.; van der Eerden, A. M. J.; Jacques, S. D. M.; Leynaud, O.; O'Brien, M. G.; Detollenaere, D.; Kaptein, R.; Weckhuysen, B. M.; Bras, W., *J. Synchrot. Radiat.* **2008,** *15*, 632-640.

52. Kim, Y.; Kim, T. Y.; Lee, H.; Yi, J., *Chem. Commun.* **2017,** *53*, 4116-4119.

53. Park, M. B.; Ahn, S. H., Ranocchiari, M. and van Bokhoven, J., *ChemCatChem.* **2017,** doi 10.1002/cctc.201700768.

54. Llabrés i Xamena, F. X.; Fisicaro, P.; Berlier, G.; Zecchina, A.; Palomino, G. T.; Prestipino, C.; Bordiga, S.; Giamello, E.; Lamberti, C., *J. Phys. Chem. B* **2003,** *107*, 7036-7044.

55. Prestipino, C.; Berlier, G.; Xamena, F.; Spoto, G.; Bordiga, S.; Zecchina, A.; Palomino, G. T.; Yamamoto, T.; Lamberti, C., *Chem. Phys. Lett.* **2002,** *363*, 389-396.

56. Lamberti, C.; Bordiga, S.; Salvalaggio, M.; Spoto, G.; Zecchina, A.; Geobaldo, F.; Vlaic, G.; Bellatreccia, M., *J. Phys. Chem. B* **1997,** *101*, 344-360.

57. Groothaert, M. H.; van Bokhoven, J. A.; Battiston, A. A.; Weckhuysen, B. M.; Schoonheydt, R. A., *J. Am. Chem. Soc.* **2003,** *125*, 7629-7640.

58. Kau, L. S.; Spirasolomon, D. J.; Pennerhahn, J. E.; Hodgson, K. O.; Solomon, E. I., *J. Am. Chem. Soc.* **1987,** *109*, 6433-6442.

59. Sano, M.; Komorita, S.; Yamatera, H., *Inorg. Chem.* **1992,** *31*, 459-463.

60. Solomon, E. I.; Heppner, D. E.; Johnston, E. M.; Ginsbach, J. W.; Cirera, J.; Qayyum, M.; Kieber-Emmons, M. T.; Kjaergaard, C. H.; Hadt, R. G.; Tian, L., *Chem. Rev.* **2014,** *114*, 3659-3853.

61. Paolucci, C.; Di Iorio, J. R.; Ribeiro, F. H.; Gounder, R.; Schneider, W. F., *Adv. Catal.* **2016,** *59*, 1-107.

62. Larsen, S. C.; Aylor, A.; Bell, A. T.; Reimer, J. A., *J. Phys. Chem.* **1994,** *98*, 11533-11540.

63. Palomino, G. T.; Fisicaro, P.; Bordiga, S.; Zecchina, A.; Giamello, E.; Lamberti, C., *J. Phys. Chem. B* **2000,** *104*, 4064-4073.

64. Martini, A.; Borfecchia, E.; Lomachenko, K. A.; Pankin, I.; Negri, C.; Berlier, G.; Beato, P.; Falsig, H.; Lamberti, C.; Bordiga, S., *Chem. Sci.* **2017,** doi: 10.1039/c7sc02266b.

65. Andersen, C. W.; Borfecchia, E.; Bremholm, M.; Jorgensen, M. R. V.; Vennestrom, P. N. R.; Lamberti, C.; Lundegaard, L. F.; Iversen, B. B., *Angew. Chem. Int. Ed.* **2017,** *56*, 10367-10372.

66. Göltl, F.; Sautet, P.; Hermans, I., *Cat. Today* **2016,** *267*, 41-46.

67. Giordanino, F.; Vennestrom, P. N.; Lundegaard, L. F.; Stappen, F. N.; Mossin, S.; Beato, P.; Bordiga, S.; Lamberti, C., *Dalton Trans.* **2013,** *42*, 12741-61.

68. McEwen, J. S.; Anggara, T.; Schneider, W. F.; Kispersky, V. F.; Miller, J. T.; Delgass, W. N.; Ribeiro, F. H., *Cat. Today* **2012,** *184*, 129-144.

69. Kwak, J. H.; Zhu, H. Y.; Lee, J. H.; Peden, C. H. F.; Szanyi, J., *Chem. Commun.* **2012,** *48*, 4758-4760.

70. Gao, F.; Washton, N. M.; Wang, Y. L.; Kollar, M.; Szanyi, J.; Peden, C. H. F., *J. Catal.* **2015,** *331*, 25-38.

71. Falsig, H.; Vennestrøm, P. N. R.; Moses, P. G.; Janssens, T. V. W., *Top. Catal.* **2016,** *59*, 861-865.

72. Vilella, L.; Studt, F., *Eur. J. Inorg. Chem.* **2016,** *2016*, 1514-1520.

73. Bates, S. A.; Verma, A. A.; Paolucci, C.; Parekh, A. A.; Anggara, T.; Yezerets, A.; Schneider, W. F.; Miller, J. T.; Delgass, W. N.; Ribeiro, F. H., *J. Catal.* **2014,** *312*, 87-97.

74. Woertink, J. S.; Smeets, P. J.; Groothaert, M. H.; Vance, M. A.; Sels, B. F.; Schoonheydt, R. A.; Solomon, E. I., *Proc. Natl. Acad. Sci. U.S.A.* **2009,** *106*, 18908-13.

75. Chen, P.; Root, D. E.; Campochiaro, C.; Fujisawa, K.; Solomon, E. I., *J. Am. Chem. Soc.* **2003,** *125*, 466-74.

76. Maiti, D.; Fry, H. C.; Woertink, J. S.; Vance, M. A.; Solomon, E. I.; Karlin, K. D., *J. Am. Chem. Soc.* **2007,** *129*, 264-5.

77. Gao, F.; Walter, E. D.; Kollar, M.; Wang, Y.; Szanyi, J.; Peden, C. H. F., *J. Catal.* **2014,** *319*, 1-14.

78. DuBois, J. L.; Mukherjee, P.; Collier, A. M.; Mayer, J. M.; Solomon, E. I.; Hedman, B.; Stack, T. D. P.; Hodgson, K. O., *J. Am. Chem. Soc.* **1997,** *119*, 8578-8579.

79. Henson, M. J.; Mukherjee, P.; Root, D. E.; Stack, T. D. P.; Solomon, E. I., *J. Am. Chem. Soc.* **1999,** *121*, 10332-10345.

80. Baldwin, M. J.; Ross, P. K.; Pate, J. E.; Tyeklar, Z.; Karlin, K. D.; Solomon, E. I., *J. Am. Chem. Soc.* **1991,** *113*, 8671-8679.

81. Smeets, P. J.; Hadt, R. G.; Woertink, J. S.; Vanelderen, P.; Schoonheydt, R. A.; Sels, B. F.; Solomon, E. I., *J. Am. Chem. Soc.* **2010,** *132*, 14736-8.

82. Pidko, E. A.; Hensen, E. J. M.; van Santen, R. A., *Proc. R. Soc. A-Math. Phys. Eng. Sci.* **2012,** *468*, 2070-2086.

83. Gagnon, N.; Tolman, W. B., *Acc Chem Res* **2015,** *48*, 2126-31.

84. Shiota, Y.; Yoshizawa, K., *Inorg Chem* **2009,** *48*, 838-45.

85. Jang, H. J.; Hall, W. K.; dItri, J., *J. Phys. Chem.* **1996,** *100*, 9416-9420.